

Operator Spectroscopy of Trained Lattice Samplers

Moxian Qian^{1,*}

¹*Johannes Gutenberg University Mainz, 55128 Mainz, Germany*

Trained lattice samplers are usually judged by the ensembles they generate. Here we instead analyze the trained field-space function itself: a flow-matching velocity, a diffusion score, or a normalizing-flow action residual. We project these functions onto operator bases fixed before the fit. The bases are chosen from symmetry, exact Gaussian path limits, finite-volume modes, and gauge covariance. We retain an operator sector when it lowers the held-out projection residual and survives the available rollout, observable, and negative-control tests.

For two-dimensional lattice ϕ^4 , a trained straight-flow teacher is not described by a local force basis alone. After the local transport basis, the remaining residual separates into two infrared pieces. The deflated zero-mode polynomial $P_5(M; t)$ reduces the dominant Binder-tail component, while the lowest nonzero Fourier shell $\phi_{|n|^2=1}^\perp$ reduces the finite- k correlator component. Wrong-parity zero modes, off-zero-mode probes, and random Fourier directions do not produce the same reductions.

The same projection distinguishes other sampler classes. A variance-exploding diffusion teacher follows the force-resolvent ordering predicted by the free theory at low-to-moderate noise. A collapsed reverse-KL normalizing flow shows a forbidden odd zero-mode term in $\Delta S_q = -\log q_\theta - S - C$, with the odd-block R^2 dropping from 0.865 to below 10^{-3} after imposing Z_2 symmetry. For gauge-equivariant teachers, the scalar basis is replaced by Lie-algebra-valued loop forces; Wilson-loop-force operators lower the tangent-field residual whereas raw-link, shuffled, and random controls do not. The operator basis is model- and symmetry-dependent, but the test is the same: project the trained field-space function, retain sectors that lower the held-out residual, and discard sectors that fail the available controls.

I. INTRODUCTION

Neural samplers for lattice field theory are usually evaluated by the ensembles they generate: susceptibilities, Binder cumulants, correlators, plaquettes, or Wilson loops are compared with Hybrid Monte Carlo (HMC) [1] or Metropolis references [2]. Observable tests are necessary, but they leave the field-space structure of the trained velocity, score, or learned density unresolved.

Flow-based, flow-matching, diffusion-based, and gauge-equivariant samplers have made neural generative models practical for lattice Monte Carlo [3–9]. Here we analyze the fixed function represented by the trained network. A flow-matching sampler represents a velocity field on configuration space; a diffusion sampler represents a score field; a normalizing flow induces a density whose mismatch with the target can be written as a scalar action residual.

The question is which lattice operators appear in these trained functions. A single operator list is not expected to apply uniformly across probability paths, symmetries, volumes, and objectives. The tests below are concrete: after the allowed directions are fixed from symmetry and limiting theory, the projection separates residual sectors that can be checked against observables and controls.

This projection, together with its control tests, defines *operator spectroscopy*. For a trained velocity, score, or learned-action residual,

$$\mathcal{T}_\theta(\tau, \phi) = \sum_{n=1}^K c_n(\tau) \mathcal{O}_n[\phi] + r_\theta(\tau, \phi). \quad (1)$$

Here τ is the probability-path coordinate for flow matching or diffusion (t or σ); for the static normalizing-flow residual ΔS_q , the path argument is absent. The operators \mathcal{O}_n are chosen before the fit, and the residual r_θ measures what the dictionary has missed. The coefficients are projection coordinates of the trained function; τ labels the FM or DM probability path.

The projection is evaluated on the trained tangent field, using held-out residuals, student-rollout errors, trajectory distances, and controls. HMC observables identify which projected sectors carry visible physical bias; when the teacher is offset from HMC, the representation tracks that teacher-level structure.

The results fall into four groups.

(i) Probability paths select different leading operator hierarchies. The exactly solvable Gaussian limits show that straight flow matching is transport-resolvent, while variance-exploding diffusion is force-resolvent (Sec. III).

(ii) In two-dimensional lattice ϕ^4 , the trained flow-matching velocity contains finite-volume collective structure beyond local force information: zero-mode operators $M, M^3, P_5(M; t)$ and the lowest soft shell $\phi_{|n|^2=1}^\perp$ reduce distinct trained-teacher residual components. The channel selectivity is visible directly in the trained-teacher residual shell spectrum. Wrong-parity, off-zero-mode, and random controls fail, while Z_2 symmetrization and a hard- Z_2 -equivariant retrain show that the identified odd dictionary is not driven by the small Z_2 -even leakage of the canonical non-equivariant FlowUNet (Sec. IV).

(iii) The projection also extends beyond the flow-matching teacher. A conditional variance-exploding diffusion teacher follows the force-resolvent ladder predicted by its probability path (Sec. V), while reverse-KL

* mqian@students.uni-mainz.de

normalizing-flow collapse appears as a forbidden Z_2 -odd zero-mode term in the learned-action residual (Sec. VI).

(iv) For gauge-covariant samplers the scalar operator dictionary is replaced by Lie-algebra-valued loop-force structures. Equivariance fixes the kinematic function space; the projection tests which covariant directions the trained dynamics actually use (Sec. VII). The gauge projection is evaluated on the trained tangent field; sampler-level Wilson-loop offsets are reported below and in the appendices.

The decomposition in Eq. (1) is not unique: basis choices and deflation conventions redistribute weight among overlapping operator sectors. Sector interpretation uses the associated residuals, rollouts, observables, and controls. The examples below use different operator lists. In each case we ask which residual component is reduced, which observable moves, and which control fails.

II. OPERATOR SPECTROSCOPY OF LEARNED GENERATIVE DYNAMICS

At fixed path coordinate τ , we compare the trained function $\mathcal{T}_\theta(\tau, \phi)$ with a linear combination of operator fields evaluated on a held-out matching distribution. The matching distribution is the interpolated FM distribution, the noised-data DM distribution, or the HMC evaluation ensemble for the static NF residual. The operator dictionaries are fixed before this comparison: symmetry, exact free-path limits, finite-volume collective-coordinate arguments, and gauge covariance determine the candidate sectors.

A. Learned objects

Let $p_t(\phi)$ be a probability path connecting a simple source distribution p_0 to a target distribution p_1 . Any deterministic probability flow obeys

$$\partial_t p_t(\phi) + \nabla_\phi \cdot [p_t(\phi) v_t(\phi)] = 0. \quad (2)$$

Different generative paths choose different natural tangent fields. The projection is applied to the trained field, not to the path action. We work with three cases:

$$\begin{aligned} \text{flow matching: } & \mathcal{T}_\theta(t, \phi) = v_\theta(t, \phi), \\ \text{diffusion: } & \mathcal{T}_\theta(\sigma, \phi) = s_\theta(\sigma, \phi) \approx \nabla_\phi \log p_\sigma(\phi), \\ \text{NF residual: } & \mathcal{T}_\theta(\phi) = \Delta S_q(\phi), \\ & \Delta S_q(\phi) = -\log q_\theta(\phi) - S(\phi) - C. \end{aligned} \quad (3)$$

The first two are vector fields; the third is a scalar action residual. A normalizing flow is implemented as an invertible map $z \sim p_0(z)$, $\phi = f_\theta(z)$, inducing

$$q_\theta(\phi) = p_0(f_\theta^{-1}(\phi)) \left| \det J_{f_\theta^{-1}}(\phi) \right|. \quad (4)$$

In the normalizing-flow case we do not project the map f_θ itself; we project the learned-action residual of the

induced density. After training, θ is fixed; the projection is applied to that fixed function.

B. Projection problem

Let $\mathcal{T}_\theta(\tau, \phi)$ generically denote one of the learned objects and let $\rho_{\text{match}}(\tau)$ be the reference distribution used for the projection audit. For FM, $\rho_{\text{match}}(t)$ is the held-out distribution of interpolated configurations $\phi_t = (1-t)\phi_0 + t\phi_1$. For DM, $\rho_{\text{match}}(\sigma)$ is the held-out noised-data distribution at noise level σ . For the static NF residual, ρ_{match} is the HMC evaluation distribution on which ΔS_q is audited. Given an operator dictionary $\{\mathcal{O}_n\}$, the matching coefficients are

$$c^*(\tau) = \arg \min_c \left\langle \left\| \mathcal{T}_\theta(\tau, \phi) - \sum_n c_n(\tau) \mathcal{O}_n[\phi] \right\|^2 \right\rangle_{\rho_{\text{match}}(\tau)}. \quad (5)$$

The fitted operator representation is

$$\mathcal{T}_{\text{rep}}(\tau, \phi) = \sum_{n=1}^K c_n^*(\tau) \mathcal{O}_n[\phi]. \quad (6)$$

The matching residual is

$$\epsilon_{\text{match}}(\tau) = \frac{\langle \|\mathcal{T}_\theta(\tau, \phi) - \mathcal{T}_{\text{rep}}(\tau, \phi)\|^2 \rangle_{\rho_{\text{match}}(\tau)}}{\langle \|\mathcal{T}_\theta(\tau, \phi)\|^2 \rangle_{\rho_{\text{match}}(\tau)}}. \quad (7)$$

Thus ϵ_{match} is a squared relative residual; the reported projection averages $\bar{\epsilon}$ are averages of this squared quantity. When quoting an RMS projection residual we write $\sqrt{\epsilon_{\text{match}}}$ or $\sqrt{\bar{\epsilon}}$ explicitly. The rollout diagnostics $\epsilon_{\text{student}}$ and D_{traj} are separate relative-norm averages, defined below. For deterministic FM rollouts we additionally use the student-rollout residual

$$\epsilon_{\text{student}}(t) = \left\langle \frac{\|v_\Gamma(t, \phi_{\text{rep}}(t)) - v_{\text{rep}}(t, \phi_{\text{rep}}(t))\|}{\|v_\Gamma(t, \phi_{\text{rep}}(t))\|} \right\rangle, \quad (8)$$

and the trajectory distance

$$D_{\text{traj}}(t) = \left\langle \frac{\|\phi_{\text{rep}}(t) - \phi_\Gamma(t)\|}{\|\phi_\Gamma(t)\|} \right\rangle. \quad (9)$$

C. Criteria for retaining an operator sector

We retain a sector when it lowers the held-out matching residual in the predicted sector, improves the corresponding rollout where a comparable rollout is available, moves the associated observable channel, and is not reproduced by symmetry-equivalent, sector-shuffled, gauge-variant, or structureless controls. When no comparable rollout diagnostic is available, the evidence is projection-level and observable-level.

D. Dictionary construction

The dictionary is built from five ingredients.

Symmetry. Restrict the function space using the symmetry of the sampler. For a Z_2 -symmetric scalar target with a symmetric source, the learned vector field is Z_2 -odd, and even zero-mode fields (M^2, M^4, \dots) are excluded as leading vector operators. Translation symmetry restricts local stencils and shell fields to translation-equivariant constructions. For gauge models, local gauge covariance restricts the tangent field to Lie-algebra-valued loop-force operators.

Free-path limit. The exactly solvable free path provides two distinct leading pairs:

$$\text{FM: } \phi, (K + \mu_t)^{-1}\phi; \quad \text{DM: } F, (I + \sigma^2 K)^{-1}F.$$

The leading basis is therefore path dependent, derived in Sec. III.

Interactions. Expanding the exact interacting conditional expectation around the Gaussian reference produces resolvent-smoothed nonlinear forces. For ϕ^4 the first correction contains cubic and Hartree-type structures, schematically $\phi^3, M^2\eta, \eta^3, \phi(\nabla\phi)^2$, with $\eta = \phi - M$. The cumulant expansion motivates these directions; whether an independent deflated component is active is determined empirically.

Zero mode. The lattice zero mode $M = V^{-1} \sum_x \phi_x$ has a Landau effective potential near a Z_2 -symmetric critical region, and its per-site force generates the odd tower M, M^3, M^5, \dots . Per-time Gram-Schmidt polynomials $P_5(M; t), P_7(M; t), \dots$ remove collinear lower-order components without changing the operator span.

Soft shells. The free resolvents amplify the lowest nonzero eigenvalues of K . After the zero mode is treated separately, the next finite-volume directions are the lowest momentum shells $|n|^2 = 1, 2, \dots$, deflated against the lower-order basis.

The basis is intentionally small and nested. Table I summarizes the dictionary used throughout the paper.

III. PATH-SELECTED OPERATOR STRUCTURE IN SOLVABLE LIMITS

The free Gaussian theory gives the first structural constraint on a trained sampler: the leading operator content depends on the probability path. This dependence is exact and architecture independent. The detailed derivations and the interacting cumulant expansion are deferred to Appendix A.

A. Straight flow matching

Consider a free lattice scalar target

$$S[\phi] = \frac{1}{2} \sum_k K(k) |\phi_k|^2, \quad p_1 = \mathcal{N}(0, K^{-1}), \quad (10)$$

with Gaussian source $p_0 = \mathcal{N}(0, I)$. Straight flow matching uses

$$\phi_t = (1-t)\phi_0 + t\phi_1. \quad (11)$$

The exact marginal velocity is

$$v_t^{\text{FM}}(\phi) = \mathbb{E}[\phi_1 - \phi_0 \mid \phi_t = \phi]. \quad (12)$$

Per Fourier mode, Gaussian conditioning gives

$$v_t^{\text{FM}}(k) = A_t(K(k)) \phi_t(k), \quad A_t(K) = \frac{t - (1-t)K}{(1-t)^2 K + t^2}. \quad (13)$$

The same kernel has the exact resolvent decomposition

$$A_t(K) = -\frac{1}{1-t} + \frac{t}{(1-t)^3} \frac{1}{K + \mu_t}, \quad \mu_t = \frac{t^2}{(1-t)^2}. \quad (14)$$

Therefore the natural free FM basis is

$$\boxed{\phi, (K + \mu_t)^{-1}\phi}. \quad (15)$$

The action force $F = -K\phi$ is not the leading FM operator; it is a local polynomial surrogate for the resolvent-filtered transport kernel. The leading learned structure of straight flow matching is therefore not the action force. It is a transport-resolvent structure selected by the path itself.

B. Variance-exploding diffusion

For a variance-exploding diffusion model, the smoothed free target at variance σ^2 is

$$p_\sigma(\phi) = \mathcal{N}(0, K^{-1} + \sigma^2 I). \quad (16)$$

The exact score is

$$s_\sigma(k) = \nabla_{\phi_k} \log p_\sigma(\phi) = -\frac{K(k)}{1 + \sigma^2 K(k)} \phi_k. \quad (17)$$

With $F_k = -K(k)\phi_k$, this is

$$s_\sigma = (I + \sigma^2 K)^{-1} F. \quad (18)$$

Thus the natural free DM hierarchy is

$$\boxed{F, (I + \sigma^2 K)^{-1} F}. \quad (19)$$

Equations (15) and (19) show that diffusion learns a different leading structure from flow matching even for the same target action. The distinction is not architectural; it is path-selected.

C. Consequence for interacting theories

Equations (15) and (19) show that the leading operator hierarchy depends on the probability path, even for the

TABLE I. Sources of learned operator structure. Operator classes are grouped by the ingredients that select them: target symmetry, the exact free probability path, interacting corrections, finite-volume zero modes, soft Fourier shells, and gauge covariance. The final row lists control directions used to test parity, sector, gauge-covariance, and structureless alternatives.

Structural source	Operator class
Z_2 , translation symmetry	$\phi, F, \Delta\phi, \Delta^2\phi, \phi(\nabla\phi)^2$
Free FM kernel	$(K + \mu_t)^{-1}\phi$
Free DM kernel	$(I + \sigma^2 K)^{-1}F$
Interacting cumulant expansion	$\phi^3, M^2\eta, \eta^3$
Finite-volume Landau zero mode	$M, M^3, P_5(M; t), P_7(M; t)$
Soft finite-volume shells	$\phi_{ n ^2=1}^\perp, \phi_{ n ^2=2}^\perp$
Gauge loop-force (Sec. VII)	$V_P, V_R, V_{P2}, V_{Pol}, V_{adjP}$
Negative controls	$M^2, M^4, M_{k=1}, M_{k=(1,1)}, R^{\text{rand}}$

same target. Interactions generate resolvent-smoothed nonlinear corrections, while finite volume exposes zero-mode and soft-shell infrared directions not efficiently captured by a finite local truncation. The interacting corrections are organized by a finite cumulant expansion around the free Gaussian reference, derived in Appendix A; the finite truncation is then tested empirically with projection residuals, rollouts, and lattice observables. Two algebraic redundancies that appear in the analysis are recorded once here. First,

$$\sigma^2 K (I + \sigma^2 K)^{-1} F = F - (I + \sigma^2 K)^{-1} F, \quad (20)$$

so $\sigma^2 KRF$ is not an independent DM rung. Second, on a fixed momentum shell $|n|^2 = q$, the kernels $(K + \mu_t)^{-1}$ and $(I + \sigma^2 K)^{-1}$ act as scalars, so a resolvent-filtered single shell is redundant with the bare shell field. The finite local basis \mathcal{B}_{L3} below approximates the FM resolvent by a polynomial in the lattice Laplacian. Because the resolvent amplifies low-eigenvalue modes, the most important nonlocal remainder after the local truncation is concentrated in the finite-volume zero mode and the lowest nonzero Fourier shells. The higher- q shells then diagnose the irreducible UV remainder of the local truncation, as verified empirically in Sec. IV B. Sec. IV tests this path-selected baseline in an interacting finite-volume setting.

IV. FINITE-VOLUME OPERATOR STRUCTURE IN A LEARNED ϕ^4 FLOW-MATCHING SAMPLER

We now apply the projection to a trained straight-flow teacher for two-dimensional ϕ^4 . The local basis \mathcal{B}_{L3} captures the short-range transport component, while the remaining held-out residual has most of its low-momentum weight in the zero mode and the lowest nonzero Fourier shell. These two infrared sectors affect different observables and survive the parity, sector, random-structure, and Z_2 -symmetry audits below. Across coupling and volume, the operator classes remain stable even when the numerical coefficient curves do not transfer.

A. Setup and local path-selected baseline

We use the two-dimensional lattice ϕ^4 action

$$S[\phi] = \sum_x \left[-2\kappa \phi_x \sum_{\mu=1}^2 \phi_{x+\hat{\mu}} + (1 - 2\lambda)\phi_x^2 + \lambda\phi_x^4 \right], \quad (21)$$

with periodic boundary conditions. The force is

$$F_x[\phi] = 2\kappa \sum_{\pm\mu} \phi_{x+\hat{\mu}} - 2(1 - 2\lambda)\phi_x - 4\lambda\phi_x^3. \quad (22)$$

All HMC, observable, and projection calculations use the same action and force convention.

The benchmark teacher is a straight-flow UNet trained on HMC samples at $L = 8$, $\kappa = 0.27$, $\lambda = 0.022$; coupling and volume checks use the datasets listed in the appendices.

The local transport surrogate suggested by the free FM limit is

$$\mathcal{B}_{L3} = \{\phi, F, \Delta\phi, \Delta^2\phi, \phi(\nabla\phi)^2\}. \quad (23)$$

This basis is the local baseline; the zero mode is added separately. Define

$$M[\phi] = \frac{1}{V} \sum_x \phi_x. \quad (24)$$

As vector-field operators, M, M^3, P_5, P_7, \dots are spatially constant fields broadcast to every lattice site. In the main text we use the sector-balanced convention

$$\chi \equiv \chi_{\text{sign}} = V(\langle M^2 \rangle - \langle M \rangle^2), \quad (25)$$

The leading zero-mode basis is

$$\mathcal{B}_{L4} = \mathcal{B}_{L3} \cup \{M, M^3\}. \quad (26)$$

B. Zero-mode and soft-shell operator structure

Residual audits split the local-basis remainder into two infrared components: the odd zero-mode tower reduces the Binder-tail component, and the lowest nonzero Fourier shell reduces the finite- k correlator component. At $L = 8$, the two directions are nearly orthogonal in both observables and the trained-teacher residual spectrum.

The \mathcal{B}_{L4} basis absorbs the leading zero-mode direction, but it leaves three sensitive residuals: the Binder cumulant U_4 , the connected correlator $G(2)$, and the structure factor $S(k_{\min})$. These observables are not meant to exhaustively validate the sampler; they are chosen because they are selectively sensitive to the zero-mode and lowest-shell sectors left unresolved by the local basis.

For a candidate operator O , its deflated version with respect to a baseline \mathcal{B} is

$$O^\perp(t, \phi) = O(\phi) - \text{Proj}_{\mathcal{B}}^{\rho_{\text{match}}(t)} O(\phi). \quad (27)$$

The projection is calibrated once on $\rho_{\text{match}}(t)$ and is not recomputed during rollout. This isolates the candidate's independent direction relative to the baseline.

Raw monomials M, M^3, M^5, \dots are highly collinear on $\rho_{\text{match}}(t)$. We define per- t Gram-Schmidt polynomials

$$P_1(M) = M, \quad (28)$$

$$P_3(M; t) = M^3 - a_{31}(t)M, \quad (29)$$

$$P_5(M; t) = M^5 - a_{53}(t)P_3(M; t) - a_{51}(t)P_1(M), \quad (30)$$

with $\langle P_i P_j \rangle_{\rho_{\text{match}}(t)} = 0$ for $i \neq j$. Adding $P_5(M; t)$ to \mathcal{B}_{L4} selectively reduces the zero-mode residual and moves U_4 toward the teacher/HMC value without changing $G(2)$ or $S(k_{\min})$.

The free FM resolvent predicts sensitivity to soft Fourier modes. On a finite lattice define

$$\phi_{|n|^2=q} = \mathcal{F}^{-1} \left[\mathbf{1}_{n_x^2+n_y^2=q} \hat{\phi}_n \right], \quad (31)$$

and

$$\phi_{|n|^2=q}^\perp = \phi_{|n|^2=q} - \text{Proj}_{\mathcal{B}_{L4}}^{\rho_{\text{match}}(t)} \phi_{|n|^2=q}. \quad (32)$$

At $L = 8$, $q = 1$ is the lowest nonzero momentum shell. Adding $\phi_{|n|^2=1}^\perp$ selectively reduces $G(2)$ and $S(k_{\min})$ but leaves U_4 unchanged. We denote the combined next-to-leading basis by

$$\mathcal{B}_{\text{NLO}} = \mathcal{B}_{L4} \cup \{P_5(M; t), \phi_{|n|^2=1}^\perp\}.$$

After both NLO channels are added (Table II), the finite- k observables $G(2)$ and $S(k_{\min})$ track the trained UNet teacher within the quoted bootstrap uncertainty, while U_4 is reduced to an $\mathcal{O}(1\sigma)$ HMC deviation. The NLO representation gives sector-level trained-teacher matching; it inherits the teacher finite- k offset and leaves a small Binder offset.

Two additional physically motivated blocks are negative or weak. A Hartree-like block built from $M^2\eta_x$, $M^2\Delta\eta_x$,

$M(\eta_x^2 - \overline{\eta^2})$, and $\eta_x^3 - \overline{\eta^3}$ is redundant after deflation against \mathcal{B}_{L4} . A mid-range stencil block built from $\Delta_{\text{diag}}\phi$, $\Delta_{\text{diag}}^2\phi$, $\phi^2\Delta\phi$, and $\phi(\Delta\phi)^2$ improves $G(2)$ only weakly compared with the lowest-shell operator.

Trained-teacher shell residuals. The NLO channel interpretation can be tested directly on the trained-teacher residual

$$r_\theta(t, \phi) = v_\theta(t, \phi) - v_{\text{rep}}(t, \phi). \quad (33)$$

We decompose r_θ into Fourier shells and compare the nested basis ladder \mathcal{B}_{L3} , \mathcal{B}_{L4} , $\mathcal{B}_{L4} + P_5$, $\mathcal{B}_{L4} + \phi_{|n|^2=1}^\perp$, and full \mathcal{B}_{NLO} (Fig. 2). The result is channel-selective: adding P_5 reduces the zero-mode shell residual without affecting the lowest nonzero shell, whereas $\phi_{|n|^2=1}^\perp$ reduces the lowest-shell residual without affecting the zero shell. At finite volume the two channels are essentially orthogonal. The higher- q shells stay flat across all five rungs and identify the irreducible UV remainder of the local truncation.

C. Control tests

The sector assignments of Sec. IV B are supported by negative controls, seed and coupling robustness, and symmetry audits of the trained teacher; full numerical tables are collected in Appendix D.

Negative controls. Starting from \mathcal{B}_{L3} we add a single candidate operator and record the residual reduction

$$\Delta_{\text{red}}\epsilon_{\text{match}} = 1 - \frac{\overline{\epsilon_{\text{match}}}[\mathcal{B}_{L3} + \{O\}]}{\overline{\epsilon_{\text{match}}}[\mathcal{B}_{L3}]}; \quad (34)$$

positive values denote percentage reduction relative to the $L3$ baseline. Wrong Z_2 parity (M^2, M^4), off-zero-mode Fourier probes ($M_{k=1}, M_{k=(1,1)}$), and structureless R^{rand} all yield $< 0.1\%$ reduction, whereas physical zero-mode additions (M, M^3) reduce the residual by large factors (Table IV). The complementary soft-shell channel is tested directly by Fig. 2.

Seed and coupling robustness of the NLO channels. The canonical NLO numbers in Table II use one trained FlowUNet at $(L, \kappa, \lambda) = (8, 0.27, 0.022)$. We repeat the same projection ladder for two additional seeds at that point and for a stronger coupling $\lambda = 0.05$ (reduced projection settings recorded in the release manifest). In every case, P_5 moves the Binder channel without affecting $G(2)$, while $\phi_{|n|^2=1}^\perp$ moves $G(2)$ and $S(k_{\min})$ without affecting U_4 ; seed-to-seed scatter of the final NLO values lies below the bootstrap uncertainty of Table II (Table V).

Z_2 violation of the trained teacher. For an exact Z_2 -symmetric target action and a Z_2 -symmetric source distribution, the FM target velocity is Z_2 -odd. We measure how far the trained, non-equivariant FlowUNet deviates by the even-part ratio

$$\epsilon_{Z_2}(t) = \frac{\langle \|v_\theta(t, \phi) + v_\theta(t, -\phi)\|^2 \rangle}{4 \langle \|v_\theta(t, \phi)\|^2 \rangle}. \quad (35)$$

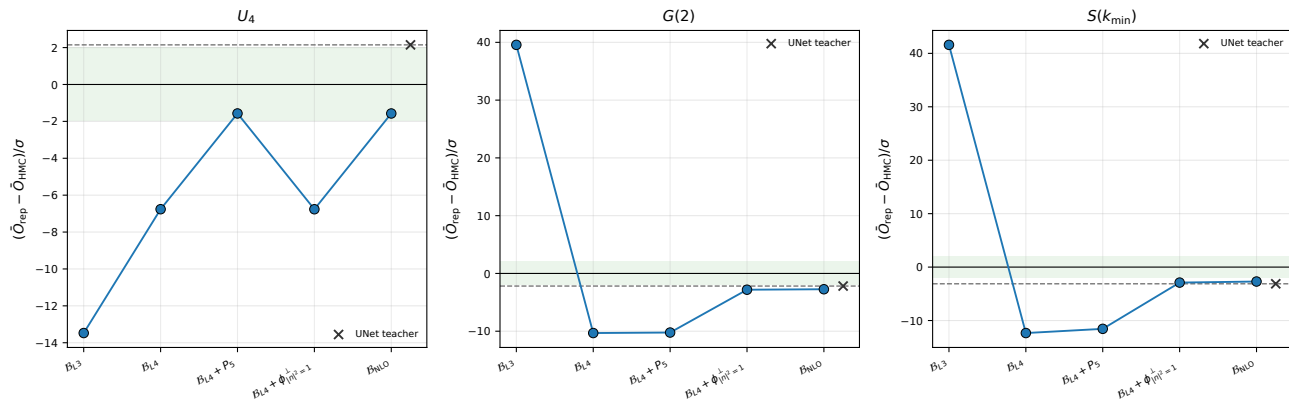


FIG. 1. NLO channel decomposition on $L = 8$, $\kappa = 0.27$. Markers show deviations from HMC in bootstrap error units. $P_5(M; t)$ selectively reduces the Binder-tail U_4 deviation but leaves $G(2)$ and $S(k_{\min})$ unchanged. $\phi_{|n|^2=1}^\perp$ selectively reduces $G(2)$ and $S(k_{\min})$ deviations but leaves U_4 unchanged. The two NLO channels are essentially orthogonal at $L = 8$; the final \mathcal{B}_{NLO} representation tracks the trained teacher in the finite- k channels and brings U_4 into an $\mathcal{O}(1\sigma)$ HMC-deviation window, while the teacher itself retains a residual 2–3 σ HMC offset.

TABLE II. Canonical $L = 8$, $\kappa = 0.27$, $\lambda = 0.022$ NLO summary. Numbers are bootstrap means over $N_{\text{boot}} = 200$ resamples; σ -distances combine representation and HMC bootstrap errors in quadrature. D_{traj}^{\max} is evaluated along the representation-driven trajectory. Pipeline and artifact details are recorded in the release manifest.

Basis	dim	$\bar{\epsilon}_{\text{match}}$	D_{traj}^{\max}	U_4 (σ)	$G(2)$ (σ)	$S(k_{\min})$ (σ)
HMC	—	—	—	0.4941 (—)	0.04332 (—)	162.6 (—)
UNet teacher	—	—	—	0.5061 (+2.1)	0.03958 (−2.2)	153.4 (−3.1)
\mathcal{B}_{L^3}	5	0.0964	0.499	−0.0184 (−13.5)	0.16465 (+39.6)	409.4 (+41.6)
\mathcal{B}_{L^4}	7	0.0077	0.113	0.4419 (−6.8)	0.02759 (−10.3)	133.1 (−12.3)
$\mathcal{B}_{L^4} + P_5(M; t)$	8	0.0064	0.090	0.4836 (−1.6)	0.02766 (−10.2)	133.1 (−11.6)
$\mathcal{B}_{L^4} + \phi_{ n ^2=1}^\perp$	8	0.0067	0.108	0.4419 (−6.8)	0.03876 (−2.8)	154.9 (−2.9)
$\mathcal{B}_{L^4} + P_5 + \phi_{ n ^2=1}^\perp$	9	0.0054	0.084	0.4836 (−1.6)	0.03883 (−2.7)	154.9 (−2.7)

For the trained $L = 8$, $\kappa = 0.27$ FlowUNet, $\overline{\epsilon_{Z_2}}$ is of order 10^{-3} on the t -grid. The leakage is structured: it loads the forbidden Z_2 -even tower $\{M^2, M^4, M^6, \phi_x^2\}$, while $R_{\text{even} \rightarrow \text{odd}}^2 \leq 0.4\%$ on the odd dictionary \mathcal{B}_{NLO} , so the even component cannot mimic the odd operator content.

Symmetry and stability checks. Define the symmetrized teacher

$$v_\theta^{\text{sym}}(t, \phi) = \frac{1}{2} [v_\theta(t, \phi) - v_\theta(t, -\phi)], \quad (36)$$

which is exactly Z_2 -odd by construction. Post-hoc projection onto v_θ^{sym} removes the even leakage while shifting core dictionary coefficients at the percent level; the matching residual drops because the even part of v_θ is forbidden by the odd basis (Table VI). Retraining a hard- Z_2 -equivariant FlowUNet from scratch ($\epsilon_{Z_2} \equiv 0$) preserves the same odd operator sectors. Likewise, a train/test split of $\rho_{\text{match}}(t)$ gives indistinguishable held-out residuals at the precision relevant here. The corresponding audit artifacts are listed in the reproducibility manifest.

D. Robustness across coupling and volume

The operator structure identified at the canonical $(L, \kappa, \lambda) = (8, 0.27, 0.022)$ point is now tested for robustness across coupling and across volume.

Coupling dependence is low rank but not rank one. For each κ in

$$\{0.22, 0.24, 0.26, 0.27, 0.28, 0.30\}, \quad (37)$$

we fit operator coefficients $c_n(t, \kappa)$ and construct

$$C_{(n,t),\kappa} = c_n(t, \kappa). \quad (38)$$

A scalar rescaling model,

$$c_n(t, \kappa) = r(\kappa)c_n(t, \kappa_0), \quad (39)$$

is rank one. The SVD is applied after the independent per- κ projections have been fitted. The coefficient surface is low rank but not rank one: the leading singular direction captures $\gtrsim 92\%$ of the coefficient energy, while the rank-one truncation nevertheless fails at the sampler level—the rank-one rollout sign-flips U_4 and collapses χ by more than an order of magnitude relative to the canonical HMC

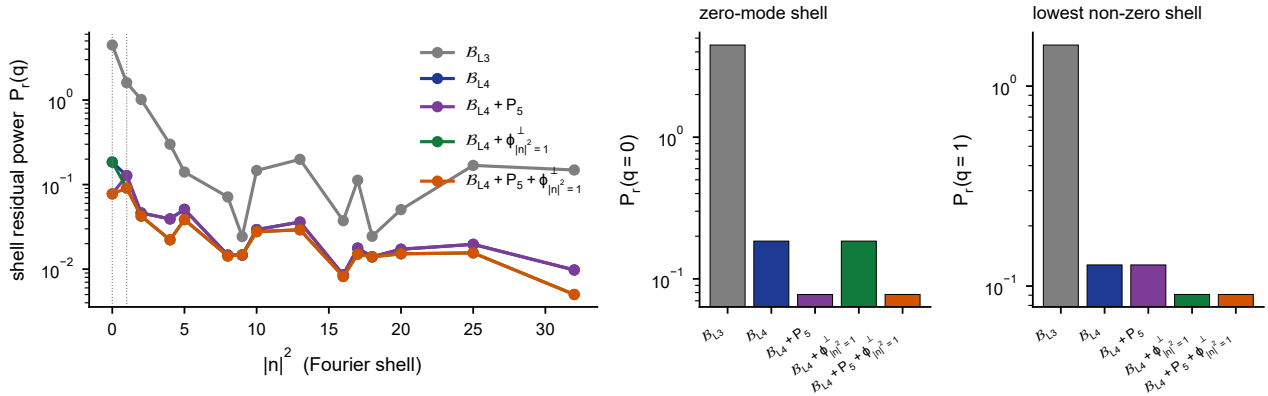


FIG. 2. Trained-teacher residual shell spectrum at $L = 8$, $\kappa = 0.27$, $\lambda = 0.022$, on a held-out matching batch. Left: residual power $P_q[r_\theta]$ versus $|n|^2$ along the five-rung ladder. Centre: P_5 suppresses the zero-mode shell without affecting the lowest nonzero shell. Right: $\phi_{|n|^2=1}^\perp$ suppresses the lowest nonzero shell without affecting the zero shell. Powers are unnormalized; the \mathcal{B}_{L3} baseline can exceed unity because the LSQ fit absorbs the missing zero-mode signal through the only available channels, an artifact that disappears at \mathcal{B}_{L4} .

reference ($U_4^{\text{HMC}} \approx 0.494$, $\chi^{\text{HMC}} \approx 59$). Adding further singular directions improves the rollout observables, with an observable-dependent useful rank. The full SVD energy fractions and rank-one rollout failures are reported in Table VII of Appendix E.

To check whether the fitted sectors vary smoothly with coupling, we inspect the projection coefficients directly as functions of both flow time and κ . Across the four representative operator sectors of the $\mathcal{B}_{L4} + \phi_{|n|^2=1}^\perp$ basis—the local force F , the Laplacian stencil $\Delta\phi$, the zero mode M , and the deflated lowest shell $\phi_{|n|^2=1}^\perp$ —the curves vary smoothly with both t and κ , supporting the use of a common operator basis across the sweep (see Fig. 9 and Fig. 8 of Appendix E).

Predictive content and limits of the coefficient surface. Smoothness of $c_n(t, \kappa)$ is necessary but not sufficient for extrapolation. We hold out $\kappa^* = 0.27$: the \mathcal{B}_{L4} coefficient functions are fitted on the five anchor couplings $\kappa \in \{0.22, 0.24, 0.26, 0.28, 0.30\}$, cubic-spline interpolated to κ^* , and rolled out without using the teacher velocity at the held-out point. The result separates local and zero-mode extrapolation: the local/action observable $\langle S \rangle / V$ is predicted to within about 3%, whereas zero-mode-dominated observables ($\langle |M| \rangle, U_4, \chi$) miss by 13–18%. The interpolated coefficients retain local-action information, but they do not predict the critical zero-mode sector. The full holdout numbers are reported in Table VIII of Appendix E; they use a separate 2000-sample HMC re-run that is not bit-identical to the canonical 8000-sample reference of Table II.

Size scaling: operator classes transfer, coefficients do not. We next compare $L = 8$ and $L = 16$ at $\kappa = 0.27$, $\lambda = 0.022$. This separates two questions: whether coefficient functions can be copied across volumes, and whether the operator classes themselves remain the right directions after rematching.

Applying $L = 8$ coefficient curves directly at $L = 16$ fails, even when the operators are redefined and re-deflated on the target lattice. After rematching the coefficients at $L = 16$, however, the same operator classes remain the active directions: $P_5(M; t)$ moves the Binder channel toward HMC, the softest nonzero shell $\phi_{|n|^2=1}^\perp$ moves the finite- k observables toward HMC, and the fixed-momentum projector $\phi_{|n|^2=4}^\perp$ does not. Thus operator-class transfer holds across the volume change, while substantial HMC residuals remain in all three observable channels even at the deepest rung tested. Size transfer is established at the level of operator classes rather than numerical coefficients.

At $L = 16$, residuals remain after adding P_5 and $\phi_{|n|^2=1}^\perp$. A predefined higher-order ladder adds $P_7(M; t)$ and the next soft shell $\phi_{|n|^2=2}^\perp$. This confirms that P_7 further moves the Binder tail toward HMC, while $\phi_{|n|^2=2}^\perp$ further moves the $|n|^2 = 2$ structure factor; the rematched $L = 16$ residual HMC offsets remain after the deepest rung. The full numerical ladder is reported in Appendix F 2 and Fig. 11. The cross-size visualization of operator-class transfer at $L = 8$ and $L = 16$ is shown in Fig. 10 of Appendix F.

V. DIFFUSION FOLLOWS A FORCE-RESOLVENT OPERATOR STRUCTURE

The free calculation predicts a different ordering for VE diffusion: the leading nonlocal correction is $R_\sigma F$, not the FM transport resolvent. We test this ordering on a conditional VE teacher for $L = 8$ ϕ^4 . The diffusion experiment tests the force-resolvent ordering of the trained score.

We use a conditional VE diffusion teacher [9–14] trained on $L = 8$, $\kappa \in \{0.26, 0.27, 0.28\}$, $\lambda = 0.022$, with zeros

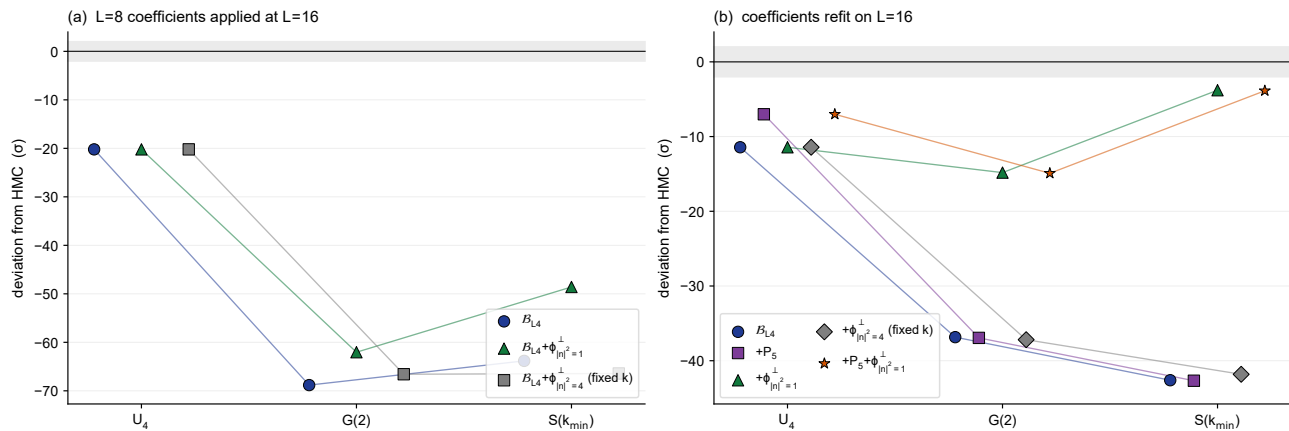


FIG. 3. Size transfer separates coefficients from operator classes. (a) Applying $L = 8$ coefficients at $L = 16$ fails for all tested observables. (b) After rematching coefficients at $L = 16$, the same operator classes move the same channels toward HMC: P_5 improves U_4 , the softest shell improves $G(2)$ and $S(k_{\min})$, whereas the fixed-physical-momentum shell remains ineffective. The shaded band marks $|z| < 2$ in combined bootstrap standard deviations from HMC; many $L = 16$ points sit well outside this band.

padding, uniform noise-time training and EMA parameter averaging, three- κ joint conditioning, and predictor-corrector sampling at SNR 0.05 (“DM-v2-C”). At $\kappa = 0.27$ the teacher reproduces the collective and infrared observables at the $\mathcal{O}(1\sigma)$ level relative to HMC, with the leading IR shell at -1.40σ and a small but statistically significant local-amplitude bias on $\langle \phi^2 \rangle$ ($\sim 2.6\%$). Because this teacher used zeros padding, the DM audit is used as a path-ordering and hierarchy check.

We project the trained score onto the predefined DM operator ladder

$$F \rightarrow F + R_\sigma F \rightarrow +\phi^3 \rightarrow +\phi^3 + M + M^3, \quad (40)$$

where $R_\sigma = (I + \sigma^2 K_{\text{eff}})^{-1}$ and $K_{\text{eff}} = m_{\text{eff}}^2 I + 2\kappa(-\Delta)$ is a regulated quadratic kernel. In this ladder F denotes the full local ϕ^4 force of Eq. (22), which already contains the onsite cubic term $-4\lambda\phi_x^3$, not only the free force $F_0 = -K\phi$. The additional ϕ^3 column is therefore an *onsite cubic reweighting direction*, allowing the learned score to depart from the fixed action-gradient coefficient of the cubic piece.

Following Eq. (20), we treat $\sigma^2 KR_\sigma F$ as a numerical-stability diagnostic only, since it lies in the same span as $\{F, R_\sigma F\}$. With its inclusion the linear-resolvent fit becomes ill-conditioned, while $\bar{\epsilon}_{\text{match}}$ is unchanged by construction. We therefore count $F + R_\sigma F$ as a single rung.

At each fixed σ , the force-resolvent and NLO rungs reduce the residual relative to weaker bases, with the dominant first reduction coming from $F \rightarrow F + R_\sigma F$ (Fig. 4). The absolute residual grows with σ : the full-NLO $\bar{\epsilon}_{\text{match}}$ ranges from $\approx 5.9 \times 10^{-3}$ at $\sigma = 0.5$ to $\approx 10^{-1}$ at $\sigma = 5$, where larger noise mixes increasingly nonlinear field configurations and the finite NLO truncation becomes less accurate. This supports the force-resolvent ordering at low-to-moderate noise and exposes the trun-

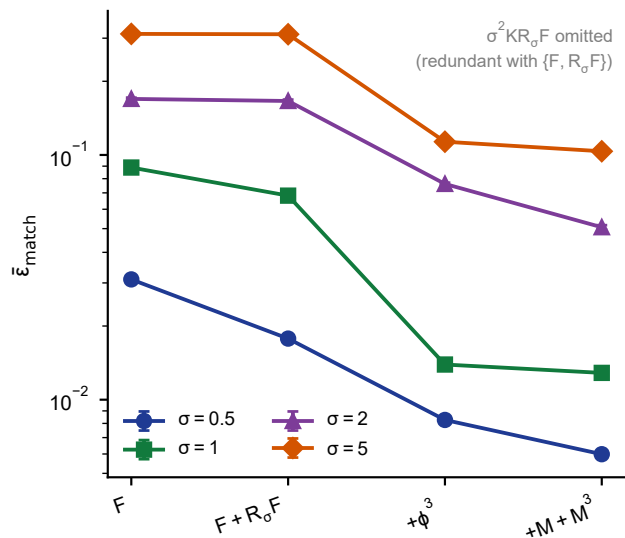


FIG. 4. Diffusion force-resolvent ladder. The redundant $\sigma^2 KR_\sigma F$ column is omitted because it lies in the span of $\{F, R_\sigma F\}$. At fixed σ , the resolvent rung and the NLO reweighting/zero-mode rungs reduce $\bar{\epsilon}_{\text{match}}$; the absolute residual grows at large σ because a finite NLO truncation is less accurate at high noise.

cation limit at large σ . The DM audit therefore focuses on the force-resolvent hierarchy of the trained score.

VI. FAILURE STRUCTURE OF REVERSE-KL NORMALIZING FLOWS

Reverse-KL sector collapse leaves a simple signature in the learned-action residual. For normalizing flows [3,

8, 15–17] trained against $\text{KL}(q_\theta||p)$ [18] with a unimodal Gaussian base, sector collapse in the broken phase is not merely an observable-level imbalance: in the learned-action residual ΔS_q of Eq. (42) it appears as a forbidden Z_2 -odd zero-mode structure. We study this in a controlled architecture-and-seed example.

We train three normalizing flows on the same $L = 8$, $\kappa = 0.27$, $\lambda = 0.022$ target, identical except for symmetry treatment: Flow A is a single-base reverse-KL flow; Flow B is a Z_2 -symmetrized version of Flow A; Flow C is a proper Z_2 -mixture trained with a log-sum-exp mixture objective. For Flow B, the density entering ΔS_q is the explicit mixture

$$q_B(\phi) = \frac{1}{2} [q_A(\phi) + q_A(-\phi)]. \quad (41)$$

Sampler observables on 4096 samples are collected in Table IX of Appendix G. Susceptibility is reported as $\chi_{\text{sign}} = V(\langle M^2 \rangle - \langle M \rangle^2)$. Flow A is collapsed to the $M < 0$ sector, while Flow B and Flow C restore sector balance. The two Z_2 branches of Flows B and C are, however, over-concentrated relative to HMC: the absolute-value susceptibility $\chi_{\text{abs}} = V(\langle M^2 \rangle - \langle |M| \rangle^2)$, reconstructed from χ_{sign} , $\langle M \rangle$, and $\langle |M| \rangle$ via $\langle M^2 \rangle = \langle M \rangle^2 + \chi_{\text{sign}}/V$, gives $\chi_{\text{abs}}^B \approx 4.7$ and $\chi_{\text{abs}}^C \approx 4.4$ versus $\chi_{\text{abs}}^{\text{HMC}} \approx 10.0$; equivalently $\langle |M| \rangle \approx 1.0$ versus 0.876 for HMC. The remaining Z_2 -balanced flow error is therefore an even-zero-mode within-sector width error, not a sector-balance error.

For each flow we compute the learned-action residual

$$\Delta S_q(\phi) = -\log q_\theta(\phi) - S(\phi) - C \quad (42)$$

on HMC samples. The constant C is chosen separately for each flow to remove the constant component on the HMC evaluation set, $\langle \Delta S_q \rangle_{\text{HMC}} = 0$. We then project ΔS_q onto a scalar operator basis grouped into odd zero-mode, even zero-mode, local-action, and soft-shell blocks. The diagnostic statistic is the block-only R^2 of the odd zero-mode block, which a Z_2 -symmetric target action cannot excite. In this grouping, the odd-zero-mode block alone gives $R_{\text{odd}}^2 = 0.865$ for the collapsed Flow A, but only 6×10^{-4} and 8×10^{-4} for the two Z_2 -respecting flows B and C. The corresponding $(R_{\text{even}}^2, R_{\text{full}}^2)$ pairs are (0.129, 0.969), (0.293, 0.382), and (0.352, 0.445). The dominant Flow A coefficients in the odd block are $c_M = +7.81$ and $c_{M^3} = +0.52$, i.e. $\Delta S_q \supset h_1 M + h_3 M^3$, the operator signature of a spurious magnetic-field term. Both Z_2 -respecting flows reduce R_{odd}^2 by three orders of magnitude.

The remaining within-sector deviation is an even-zero-mode and local-action residual. The projection localizes the sector-collapse mechanism to the forbidden odd zero-mode block.

VII. GAUGE-COINVARIANT LOOP-FORCE STRUCTURE

We finally turn to gauge-covariant tangent fields. The scalar Z_2 -odd dictionary is replaced by Lie-algebra-valued

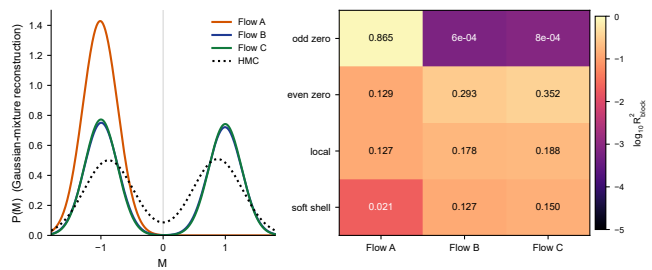


FIG. 5. Operator projection of the learned-action residual $\Delta S_q = -\log q_\theta - S - C$. The single-base reverse-KL flow has a large odd zero-mode projection, while Z_2 symmetrization and proper Z_2 -mixture training suppress this forbidden block below 10^{-3} . The left panel is a moment-matched visualization of $P(M)$, not an input to the residual projection.

loop-force operators. In $U(1)$, several of these loop-force primitives are already available to the architecture, so the projection mainly tests whether the built-in operator prior is the one the trained field uses. In $SU(2)$, the same projection tests which covariant loop-force directions carry the trained tangent field, with the adjoint-plaquette force as the dominant non-plaquette loading in the scanned checkpoint.

We use the gauge systems as tangent-field projection tests. Wilson-loop-force directions reduce the held-out residual, whereas raw-link, shuffled, and random directions do not. Sampler-level Wilson-loop offsets are reported in Appendix J and Appendix K.

A. Gauge tangent formalism

For a link field $U_{x,\mu} \in G$, $G = U(1)$ or $SU(2)$, we write the learned tangent field in left-trivialized form,

$$\dot{U}_{x,\mu} = A_{x,\mu}[U] U_{x,\mu}, \quad A_{x,\mu}[U] \in \mathfrak{g}. \quad (43)$$

Local gauge transformations $U_{x,\mu} \mapsto g_x U_{x,\mu} g_{x+\hat{\mu}}^{-1}$ require the covariance condition

$$A_{x,\mu}[U^g] = g_x A_{x,\mu}[U] g_x^{-1}, \quad (44)$$

which collapses to plain invariance for the abelian $U(1)$ case.

B. Loop-force operator dictionaries

Each Wilson-loop action term yields, by variation, a gauge-covariant Lie-algebra link tensor. We use:

$U(1)$.

$$V_P(l) = - \sum_{p \supset l} s_{p,l} \sin \theta_p, \quad (45)$$

$$V_R(l) = - \sum_{r \supset l} s_{r,l} \sin \theta_r, \quad (46)$$

$$V_{P^2}(l) = - \sum_{p \supset l} 2 s_{p,l} \sin(2\theta_p), \quad (47)$$

$$V_{\text{Pol}}(l) = - \mathbf{1}_{l \in \Theta\text{-line}} \sin \Theta_\mu(x_\perp). \quad (48)$$

$SU(2)$. Writing each plaquette as $U_p = U_l S_{p,l}$ with staple $S_{p,l}$ and TA the traceless-anti-Hermitian projection,

$$V_P(l) = \text{TA} \left(U_l \sum_{p \supset l} S_{p,l} \right), \quad (49)$$

$$V_R(l) = \text{TA} \left(U_l \sum_{r \supset l} S_{r,l} \right), \quad (50)$$

$$V_{\text{adjP}}(l) = \text{TA} \left(U_l \sum_{p \supset l} \text{Tr}(U_p) S_{p,l} \right). \quad (51)$$

At small lattice spacing $V_P \sim a^3 D_\nu F_{\nu\mu}$, V_R provides the leading higher-derivative (Symanzik) correction, and V_{adjP} is the non-abelian analogue of the higher-harmonic abelian operator V_{P^2} .

We use the following nested operator bases throughout this paper:

$$\begin{aligned} \mathcal{B}_0 &= \{V_P\}, & \mathcal{B}_1 &= \{V_P, V_R\}, \\ \mathcal{B}_2^{\text{U}(1)} &= \{V_P, V_R, V_{P^2}\}, & \mathcal{B}_2^{\text{SU}(2)} &= \{V_P, V_R, V_{\text{adjP}}\}, \\ \mathcal{B}_3^{\text{U}(1)} &= \mathcal{B}_2^{\text{U}(1)} \cup \{V_{\text{Pol}}\}. \end{aligned} \quad (52)$$

\mathcal{B}_2 refers to the symmetry-appropriate three-operator basis for the gauge group at hand. In the $U(1)$ ladder the subscript labels the rung rather than the number of operators: $\mathcal{B}_3^{\text{U}(1)}$ contains the four loop-force primitives $\{V_P, V_R, V_{P^2}, V_{\text{Pol}}\}$. The non-primitive extensions \mathcal{B}_4 and \mathcal{B}_5 used only in Appendix L build further on $\mathcal{B}_3^{\text{U}(1)}$.

C. Negative controls

To rule out arbitrary covariant-feature explanations we use three independent negative controls per system. For $U(1)$: the gauge-variant raw link θ_l , a random tangent field V_{rand} , and a shuffled-stencil plaquette force V_{shuffle} . For $SU(2)$: the raw-link projection $\text{TA}(U_l)$, a random Lie-algebra field, and a shuffled-staple operator. The controls either deliberately violate gauge covariance (the raw-link controls) or preserve the gauge-covariant tangent-field tensor shape while removing the loop-force structure (the random and shuffled-stencil controls); none of them aligns with the learned tangent.

D. Trained gauge teachers and projection results

We train denoising-score-matching teachers [10, 13] using the gauge-equivariant networks `U1EquivNet` (~ 510 k params) and `SU2EquivNet` (~ 513 k params). In the language of group-equivariant networks [19], both architectures impose the symmetry at the level of the function space: they take only gauge-invariant inputs (Wilson-loop cosines/sines) and produce gauge-covariant Lie-algebra outputs; $\bar{\epsilon}_{\text{gauge}}$ is at the numerical-audit floor by construction. HMC and heatbath sanity checks for the underlying training distributions are reported in Appendix I.

The held-out matching residuals on the Wilson-loop-force-plus-control ladder are summarized in Fig. 6; the full numerical table, including rolled-out plaquette biases, is deferred to Appendix J. In every case the gauge-equivariance violation $\bar{\epsilon}_{\text{gauge}} \lesssim 4 \times 10^{-4}$ sits at the numerical-audit floor; the per-step matching residual is reduced along the Wilson-loop-force ladder (with squared relative residual moving from $\bar{\epsilon}[\mathcal{B}_0] \sim 0.27\text{--}0.58$ to $\bar{\epsilon}_{\text{best}}^{\text{loop}} \sim 0.25\text{--}0.42$, i.e. RMS residual $\sqrt{\bar{\epsilon}} \sim 0.5\text{--}0.7$ of the trained tangent norm); and the negative controls remain within numerical noise of $\bar{\epsilon}[\mathcal{B}_0]$ (relative drift below 0.5%). Adding non-primitive operators $V_{2 \times 2}$ and $V_{|n|^2=1}^\perp$ for $U(1)$ gives only sub-percent further reduction in the per-step matching residual at the couplings tested (see Appendix L).

The full per-system numbers, including $\bar{\epsilon}_{\text{gauge}}$, the residual baseline $\bar{\epsilon}[\mathcal{B}_0]$, the deepest loop-force and best-control rungs $\bar{\epsilon}_{\text{best}}^{\text{loop}}$, $\bar{\epsilon}_{\text{best}}^{\text{neg}}$, and the rolled-out plaquette of the canonical \mathcal{B}_2 representation, are collected in Table XIII of Appendix J.

E. Equivariance vs operator content

Equivariance plays a kinematic role: it restricts the learned tangent field to the allowed function space $\mathcal{H}^G = \{A : A[U^g] = g A[U] g^{-1}\}$, but does not determine the dynamical operator content inside that space. The shuffled-stencil control V_{shuffle} , built from exactly the same plaquette-force ingredients as V_P but with the spatial stencil scrambled, is gauge covariant yet fails to reduce the matching residual. The operator projection runs *after* the symmetry constraint, and the negative controls separate dynamically relevant loop-force operators from merely covariant directions.

The architecture–projection overlap is different in $U(1)$ and $SU(2)$. For $U(1)$, the leading loop-force directions are built into `U1EquivNet`, so the projection mainly validates the operator prior and the control hierarchy. For $SU(2)$, the projection should be read conservatively as an architecture audit: it tests which covariant loop-force direction carries the trained tangent field. In the scanned checkpoint, V_{adjP} is the dominant loading while V_R is weak, and the control directions fail. Equivariance fixes the kinematic function space; the projection tests which

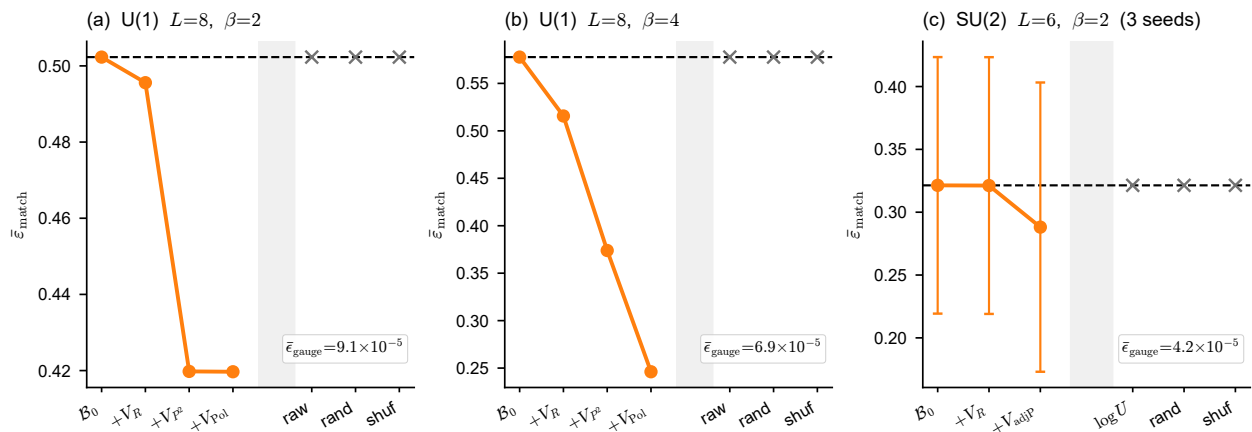


FIG. 6. Gauge operator projection. Wilson-loop-force ladders (orange, connected) reduce the held-out matching residual; the three negative controls (grey crosses) remain at the plaquette-force baseline (dashed). SU(2) error bars are the standard deviation over three audit-RNG seeds on the same trained teacher. Insets quote $\bar{\epsilon}_{\text{gauge}}$ of the trained network.

covariant directions the trained dynamics actually use.

VIII. DISCUSSION

The main lesson is that trained samplers acquire structured field-space operators, but the active sector is selected by the learned object, probability path, symmetry, interactions, and finite-volume structure rather than by a universal operator list. The fitted coefficients are coordinates of the trained velocity, score, or density residual; their numerical values depend on the matching distribution, operator normalization, and deflation convention.

A. What carries across examples

Across the examples, what carries over is a testing strategy rather than a universal operator dictionary. Straight flow matching exposes transport-resolvent directions, diffusion exposes force-resolvent directions, reverse-KL collapse appears as a forbidden zero-mode density residual, and gauge-covariant teachers expose loop-force tangent directions. Table III records, for each learned object, the retained operator directions and the residual or observable channel in which they are tested.

The negative controls sharpen the same comparison. Force-only truncations miss straight FM because the straight path is transport-resolvent. Local-only bases miss finite-volume zero-mode and soft-shell remnants. Rank-one coupling rescalings miss subleading directions in the coefficient surface. Fixed-physical-momentum projectors miss the finite-volume correction because the relevant projector follows the lowest lattice momentum shell.

B. Scope

The projections should be read at three levels. At the coefficient level, numerical values depend on normalization, deflation, the matching distribution, and the trained teacher. At the sector level, the statements are more stable: they identify which directions appear, which residuals they reduce, and which controls fail. At the sampler level, information comes from rolled-out observables and therefore depends on the teacher and the rollout procedure.

This distinction is useful in the examples above. The diffusion audit tests the force-resolvent ladder in the low-to-moderate noise range where the finite basis is accurate. The normalizing-flow audit isolates one reverse-KL collapse mechanism in the odd zero-mode block. The gauge audits pair tangent-field residuals with the corresponding Wilson-loop offsets. In each case, analytic structure supplies candidate directions, while residuals, observables, and controls determine which sector assignment is supported.

C. Outlook

The most direct extension is to apply the projection during training, so that the appearance of individual operator sectors can be tracked. A second direction is to turn measured sectors into training priors, for example by penalizing forbidden components such as the odd zero-mode residual in Sec. VI. A third is to connect the operator coordinates to parameter-space geometry by pushing Hessian or Gauss-Newton eigenmodes through the network Jacobian. Finally, a finite-step blocking study could ask how the measured sectors and coefficients transform under coarse graining; that question requires its own blocking map, conditional teachers, and operator-mixing measurements.

TABLE III. Summary across learned sampler classes. Each row lists the trained object being projected, the symmetry constraints, the operator directions retained by the projection, and the residual or observable channel in which they are tested.

System	Learned object	Symmetry	Operator directions	Main diagnostic
ϕ^4 FM	$v_\theta(t, \phi)$	Z_2 , translations	$M, M^3, P_5, \phi^\perp_{ n =1}$	$U_4, G(2), S(k_{\min})$, shell residuals
ϕ^4 DM	$s_\theta(\sigma, \phi)$	Z_2 , translations	$F, R_\sigma F, \phi^3, M, M^3$	force-resolvent ladder
ϕ^4 reverse-KL NF	$\Delta S_q = -\log q_\theta - S - C$	scalar Z_2	odd zero-mode block	$R_{\text{odd}}^2 = 0.865 \rightarrow < 10^{-3}$
U(1) gauge, $L=8$	gauge tangent field	local U(1)	$V_P, V_R, V_{P^2}, V_{\text{Pol}}$	Wilson-loop-force ladder vs gauge controls
SU(2) gauge, $L=6$	gauge tangent field	local SU(2)	V_P, V_{adjP} (V_R tested but weak)	dominant non-plaquette V_{adjP} direction

ACKNOWLEDGMENTS

The author thanks Shiyang Chen, Cunxi Gong, Biagio Lucini, Zhenkang Lu, Zhuoyi Pang, and Jianhui Zhang for helpful discussions.

DATA AND CODE AVAILABILITY

The paper source, code, and frozen artifacts will be released at github.com/qxxmax/operatormatching. An anonymized artifact package is provided for review; an archival DOI will be added upon acceptance.

Appendix A: From exact free kernels to interacting operator representations

This appendix makes precise what is exact and what is a finite operator truncation. The free Gaussian formulas are exact identities. For the interacting ϕ^4 theory, the conditional representations remain exact, but the conditional expectations are not closed-form; expanding them around the Gaussian reference produces the operator tower tested in the body of the paper.

1. Conventions

The lattice field is $\phi \in \mathbb{R}^V$, $V = L^2$. The free Gaussian reference is

$$S_0[\phi] = \frac{1}{2}\phi^T K \phi, \quad K > 0, \quad (\text{A1})$$

with covariance K^{-1} . An interacting target factorizes as

$$S[\phi] = S_0[\phi] + S_{\text{int}}[\phi], \quad (\text{A2})$$

with force $F = -\nabla S = F_0 + F_{\text{int}}$, where $F_0 = -K\phi$ and $F_{\text{int}} = -\nabla S_{\text{int}}$. In numerical projection K may be replaced by a positive regulated kernel $K_{\text{eff}} = m_{\text{eff}}^2 I + 2\kappa(-\Delta)$ when the bare quadratic part is not positive definite near criticality. Changing this scheme shifts coefficients but not operator-class statements.

2. Straight flow matching

Independent endpoints $\phi_0 \sim p_0$, $\phi_1 \sim p_1$, with $\phi_t = (1-t)\phi_0 + t\phi_1$, give the population FM minimizer

$$v_t^*(\phi) = \mathbb{E}[\phi_1 - \phi_0 \mid \phi_t = \phi]. \quad (\text{A3})$$

Setting $y = \phi_1$ and using $\phi_0 = (\phi - ty)/(1-t)$, one finds

$$v_t^*(\phi) = \frac{1}{1-t} (\mathbb{E}[y \mid \phi_t = \phi] - \phi). \quad (\text{A4})$$

For $p_0 = \mathcal{N}(0, I)$,

$$q_t(y \mid \phi) = \frac{1}{Z_t(\phi)} \exp \left[-S[y] - \frac{1}{2(1-t)^2} \|\phi - ty\|^2 \right]. \quad (\text{A5})$$

This formula is exact for any target.

For $S[y] = \frac{1}{2}y^T K y$, the exponent is quadratic and $q_t^{(0)}(y \mid \phi) = \mathcal{N}(m_t, C_t)$, with

$$\begin{aligned} C_t &= (K + \mu_t I)^{-1}, & \mu_t &= \frac{t^2}{(1-t)^2}, \\ m_t &= \frac{t}{(1-t)^2} (K + \mu_t I)^{-1} \phi. \end{aligned} \quad (\text{A6})$$

Thus

$$v_t^{(0)}(\phi) = -\frac{1}{1-t} \phi + \frac{t}{(1-t)^3} (K + \mu_t I)^{-1} \phi. \quad (\text{A7})$$

For $S = S_0 + S_{\text{int}}$, the exact interacting conditional mean is

$$\bar{y}_t(\phi) = \frac{\langle y e^{-S_{\text{int}}} \rangle_0}{\langle e^{-S_{\text{int}}} \rangle_0}, \quad (\text{A8})$$

where $\langle \cdot \rangle_0$ is expectation under $y \sim \mathcal{N}(m_t, C_t)$. To first order, $\bar{y}_t = m_t - \text{Cov}_0(y, S_{\text{int}}) + O(S_{\text{int}}^2)$. Stein's identity gives

$$\bar{y}_t = m_t + C_t \langle F_{\text{int}}[y] \rangle_0 + O(S_{\text{int}}^2), \quad (\text{A9})$$

and therefore

$$v_t = v_t^{(0)} + \frac{1}{1-t} C_t \langle F_{\text{int}} \rangle_0 + O(S_{\text{int}}^2). \quad (\text{A10})$$

For $S_{\text{int}} = \lambda \sum_x y_x^4$,

$$\delta v_t = -\frac{4\lambda}{1-t} C_t [m_t^3 + 3 \text{diag}(C_t) m_t] + O(\lambda^2). \quad (\text{A11})$$

3. Variance-exploding diffusion

For VE noising $x = y + \sigma \xi$, $\xi \sim \mathcal{N}(0, I)$,

$$q_\sigma(y | x) = \frac{1}{Z_\sigma(x)} \exp \left[-S[y] - \frac{1}{2\sigma^2} \|x - y\|^2 \right], \quad (\text{A12})$$

and Tweedie's identity gives

$$s_\sigma(x) = \nabla_x \log p_\sigma(x) = \frac{1}{\sigma^2} [\mathbb{E}[y | x] - x]. \quad (\text{A13})$$

For $S[y] = \frac{1}{2} y^T K y$, the conditional is Gaussian with

$$\begin{aligned} C_\sigma &= (K + \sigma^{-2} I)^{-1} = \sigma^2 R_\sigma, & m_\sigma &= R_\sigma x, \\ R_\sigma &= (I + \sigma^2 K)^{-1}. \end{aligned} \quad (\text{A14})$$

Thus

$$s_\sigma^{(0)}(x) = \frac{1}{\sigma^2} (R_\sigma - I)x = -R_\sigma K x = R_\sigma F_0[x]. \quad (\text{A15})$$

For the interacting target,

$$s_\sigma(x) = R_\sigma F_0[x] + R_\sigma \langle F_{\text{int}}[y] \rangle_0 + O(S_{\text{int}}^2). \quad (\text{A16})$$

For $S_{\text{int}} = \lambda \sum_x y_x^4$,

$$s_\sigma(x) = R_\sigma F_0 - 4\lambda R_\sigma [m_\sigma^3 + 3 \text{diag}(C_\sigma) m_\sigma] + O(\lambda^2). \quad (\text{A17})$$

At small σ , $R_\sigma = I - \sigma^2 K + O(\sigma^4)$, $m_\sigma = x + O(\sigma^2)$, and $\text{diag}(C_\sigma) = \sigma^2 + O(\sigma^4)$, so $s_\sigma = F + O(\sigma^2)$, as required.

4. Zero modes and soft shells

The finite-volume zero mode is $M = V^{-1} \sum_x \phi_x$. Near a Z_2 -symmetric critical region, the effective zero-mode potential takes the even Landau form

$$S_{\text{eff}}(M) = V(a_2 M^2 + a_4 M^4 + a_6 M^6 + \dots).$$

Since $\partial M / \partial \phi_x = 1/V$, the per-site force contains

$$-\frac{\partial S_{\text{eff}}}{\partial \phi_x} = -2a_2 M - 4a_4 M^3 - 6a_6 M^5 - \dots \quad (\text{A18})$$

This is the origin of the odd zero-mode tower.

The free resolvents amplify low-eigenvalue modes of K . On a finite periodic lattice the next IR-relevant directions after the zero mode are the lowest nonzero Fourier shells:

$$\phi_{|n|^2=q} = \mathcal{F}^{-1} [\mathbf{1}_{n_x^2+n_y^2=q} \hat{\phi}_n]. \quad (\text{A19})$$

We use deflated shell fields to avoid double counting with lower-order operators.

Appendix B: Action and observables

The action is Eq. (21). The hopping term counts each positive-direction nearest-neighbor pair once. The force Eq. (22) contains both forward and backward neighbors because differentiating the hopping term with respect to ϕ_x collects all terms involving ϕ_x .

We use the Binder cumulant [20]

$$M = \frac{1}{V} \sum_x \phi_x, \quad U_4 = 1 - \frac{\langle M^4 \rangle}{3\langle M^2 \rangle^2}.$$

Three susceptibilities appear in the codebase and are labeled explicitly:

$$\begin{aligned} \chi_{\text{raw}} &= V \langle M^2 \rangle, \\ \chi_{\text{sign}} &= V (\langle M^2 \rangle - \langle M \rangle^2), \\ \chi_{\text{abs}} &= V (\langle M^2 \rangle - \langle |M| \rangle^2). \end{aligned} \tag{B1}$$

They agree only when both $\langle M \rangle^2$ and $\langle |M| \rangle^2$ are negligible compared with $\langle M^2 \rangle$. At finite volume, $\langle |M| \rangle$ is generically nonzero even in a Z_2 -symmetric ensemble, so χ_{abs} and χ_{sign} differ in broken or near-critical samples.

The FM canonical NLO table reports U_4 , $G(2)$, and $S(k_{\min})$, not a susceptibility. The DM teacher diagnostic table quotes χ_{sign} . The reverse-KL table quotes χ_{sign} and reports $\langle |M| \rangle$ separately so χ_{abs} can be reconstructed.

For two-point and structure-factor observables we define

$$G_{\text{raw}}(r) = \langle \phi_x \phi_{x+r} \rangle, \quad G_{\text{conn}}(r) = \langle (\phi_x - M)(\phi_{x+r} - M) \rangle, \tag{B2}$$

and

$$S_{\text{raw}}(k) = |\hat{\phi}_k|^2, \quad S_{\text{norm}}(k) = S_{\text{raw}}(k)/V. \tag{B3}$$

For the translationally averaged estimator used here,

$$G_{\text{conn}}(r) = G_{\text{raw}}(r) - \langle M^2 \rangle. \tag{B4}$$

The FM observable tables report $G_{\text{conn}}(2)$ and $S_{\text{raw}}(k_{\min})$. The DM diagnostic table inherits the diffusion-evaluation convention and reports $G_{\text{raw}}(2)$ and $S_{\text{norm}}(k_{\min})$. Table captions label the convention used.

HMC reference checks. For all HMC datasets we record $P(M > 0)$, $\langle M \rangle$, and autocorrelations of M and $|M|$. The three susceptibilities of Eq. (B1) are reported with the convention named in each table. At $\kappa = 0.30$ the signed sector fraction is imbalanced, so χ_{sign} and χ_{abs} differ materially; sector-conditioned Z_2 -even observables, however, differ by less than a few percent.

Appendix C: Derivation and definition of the operator dictionary

The dictionary contains four types of operators: symmetry-allowed local fields, exact free-path resolvent directions, interacting cumulant corrections, and finite-volume zero-mode or soft-shell directions not efficiently captured by bounded-depth local stencils.

The ϕ^4 action and Gaussian source are invariant under $\phi \rightarrow -\phi$. For FM and DM this implies a Z_2 -odd vector field, so the vector dictionary is restricted to odd fields. Even fields may appear in scalar action residuals, as in the NF analysis, but not as leading vector operators.

The free FM kernel contains $(K + \mu_t I)^{-1} \phi$. For modes with $K(k)/\mu_t < 1$,

$$(K + \mu_t I)^{-1} \phi = \mu_t^{-1} [I - \mu_t^{-1} K + \mu_t^{-2} K^2 - \dots] \phi.$$

On the lattice, K is a polynomial in the identity and the nearest-neighbor Laplacian, so truncating this expansion generates $\phi, \Delta\phi, \Delta^2\phi, \dots$. The local force adds the action-gradient direction, and $\phi(\nabla\phi)^2$ is the lowest odd scalar-gradient coupling used in the local nonlinear sector.

The zero-mode tower follows from the Landau force $-2a_2M - 4a_4M^3 - 6a_6M^5 - \dots$. The leading pair M, M^3 defines $\mathcal{B}_{L4} = \mathcal{B}_{L3} \cup \{M, M^3\}$. Higher monomials are nearly collinear with lower ones on $\rho_{\text{match}}(t)$, so we use per-time Gram-Schmidt polynomials P_5, P_7, \dots

The derivative expansion of a resolvent fails for the lowest eigenvalues of K , which are amplified by the resolvents. On a finite periodic lattice, the eigenvectors of K are Fourier modes. After the zero mode is treated separately, the next directions are the nonzero shells $|n|^2 = 1, 2, \dots$. This explains why the active shell changes with volume: the finite-volume correction follows the softest lattice mode, not a fixed physical momentum.

Deflation is a scheme choice. For a candidate operator O and a baseline basis \mathcal{B} ,

$$O^\perp(t, \phi) = O(\phi) - \sum_m a_m(t) V_m(\phi), \quad (\text{C1})$$

$$a(t) = \arg \min_a \langle \|O - \sum_m a_m V_m\|^2 \rangle_{\rho_{\text{match}}(t)}.$$

The sector statement is that adding the corresponding operator class reduces the targeted residual or moves the corresponding observable.

Reducing ϵ_{match} alone is not sufficient. For vector-field examples, matching residual improvements are paired with available rollout diagnostics and movement of a corresponding observable in the predicted direction. Static scalar residuals are tested at projection and observable level. Negative controls include \mathbb{Z}_2 -even zero-mode fields, Hartree-type blocks deflated against \mathcal{B}_{L4} , mid-range diagonal stencils, and resolvent-filtered single shells.

Appendix D: Control tests for the scalar flow-matching audit

Tables IV–VI and Fig. 7 give the control, robustness, symmetry, and rollout checks summarized in Sec. IV C.

Negative-control audit. The full negative-control table for the $L = 8$, $\kappa = 0.27$, $\lambda = 0.022$ trained teacher, discussed in Sec. IV C, is given in Table IV.

TABLE IV. Negative-control test for the $L = 8$, $\kappa = 0.27$, $\lambda = 0.022$ operator dictionary. Each row adds one candidate block to \mathcal{B}_{L3} and refits the trained velocity. $\Delta\epsilon$ is the relative residual drop versus \mathcal{B}_{L3} .

block	symmetry / role	$\bar{\epsilon}_{\text{match}}$	$\Delta\epsilon$ vs $L3$	verdict	reason
\mathcal{B}_{L3} baseline	\mathbb{Z}_2 -odd, perturbative	0.0964	+0.0%	—	reference
+ M	\mathbb{Z}_2 -odd, zero-mode	0.0156	+83.8%	accepted	fits residual
+ M^3	\mathbb{Z}_2 -odd, zero-mode	0.0745	+22.8%	partial	small residual capture
+ $\{M, M^3\} = \mathcal{B}_{L4}$	\mathbb{Z}_2 -odd, zero-mode	0.0077	+92.0%	accepted	fits residual
+ M^2	\mathbb{Z}_2 - even (forbidden)	0.0963	+0.1%	rejected	symmetry-forbidden
+ M^4	\mathbb{Z}_2 - even (forbidden)	0.0964	+0.0%	rejected	symmetry-forbidden
+ M^5	\mathbb{Z}_2 -odd, redundant w/ M, M^3	0.0912	+5.4%	partial	small residual capture
+ $M_{k=1}$	\mathbb{Z}_2 -odd, off-zero-mode probe	0.0964	+0.0%	rejected	no residual capture
+ $M_{k=(1,1)}$	\mathbb{Z}_2 -odd, off-zero-mode probe	0.0964	+0.0%	rejected	no residual capture
+ R_{rand}	\mathbb{Z}_2 -odd, random Fourier mask	0.0964	+0.0%	rejected	no residual capture

Seed and coupling robustness. The per-seed and per- λ NLO numbers that back the robustness statement of Sec. IV D are reported in Table V.

TABLE V. Seed and coupling robustness of the ϕ^4 NLO channels.

basis	$\bar{\epsilon}_{\text{match}}$	U_4	$G(2)$	$S(k_{\min})$
$\lambda = 0.022$, three independent teachers (mean \pm std)				
\mathcal{B}_{L3}	0.0918 \pm 0.0027	0.071 \pm 0.001	0.1610 \pm 0.0047	402.6 \pm 9.3
\mathcal{B}_{L4}	0.0064 \pm 0.0012	0.435 \pm 0.011	0.0288 \pm 0.0003	136.2 \pm 1.3
+ P_3	0.0053 \pm 0.0010	0.479 \pm 0.013	0.0288 \pm 0.0003	136.0 \pm 1.2
+ $\phi_{ n ^2=1}^\perp$	0.0054 \pm 0.0012	0.435 \pm 0.011	0.0399 \pm 0.0006	157.7 \pm 0.8
NLO	0.0043 \pm 0.0010	0.479 \pm 0.013	0.0398 \pm 0.0006	157.4 \pm 0.8
HMC ($\lambda = 0.022$)	—	0.494	0.0433	162.6
$\lambda = 0.05$ contrast (single teacher)				
\mathcal{B}_{L3}	0.0402	0.067	0.0672	212.2
\mathcal{B}_{L4}	0.0093	0.239	0.0297	137.3
+ P_3	0.0093	0.254	0.0297	137.3
+ $\phi_{ n ^2=1}^\perp$	0.0071	0.239	0.0414	160.0
NLO	0.0071	0.254	0.0413	160.0
HMC ($\lambda = 0.05$)	—	0.256	0.0437	165.0

Post-hoc \mathbb{Z}_2 symmetrization. The full symmetrization (Sec. IV C) at the projection-level and rolled-out-observable level is reported in Table VI.

TABLE VI. Post-hoc Z_2 -symmetrized teacher audit on \mathcal{B}_{NLO} . Removing the forbidden even component lowers the matching residual, as expected for an odd dictionary. The fitted coefficients shift at the percent level and the rolled-out representation observables change by less than 1%.

Metric	raw v_θ	sym. v_θ^{sym}	rel. drift
$\bar{\epsilon}_{Z_2}$ mean / max	1.53×10^{-3} / 3.77×10^{-3}	–	–
$\bar{\epsilon}_{\text{match}}$	0.0054	0.0039	33.23%
$\ \Delta c\ /\ c\ $, mean over t	–	–	6.01%
<i>Rolled-out observables, representation sampler</i>			
$\langle M \rangle$	0.8545	0.8544	0.013%
U_4	0.4856	0.4857	0.014%
χ	58.0916	58.0735	0.031%
$\langle S \rangle/V$	0.3733	0.3703	0.791%

Rollout diagnostics. Figure 7 reports the rollout comparison between the canonical $L = 8$, $\kappa = 0.27$ teacher and the \mathcal{B}_{NLO} representation. The sector assignments are based on Table II and the control audit.

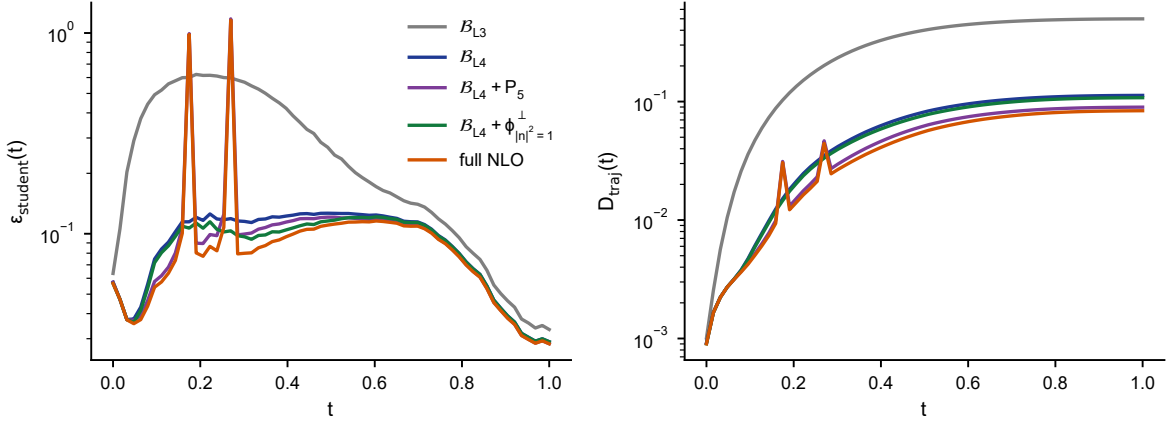


FIG. 7. Rollout diagnostics on $L = 8$. Left: $\epsilon_{\text{student}}(t)$ along the representation rollout. Right: trajectory distance $D_{\text{traj}}(t)$ to the teacher rollout. Rollout observables are reported in addition to ϵ_{match} . The sharp features arise along the representation-driven trajectory; sector evidence comes from Table II and the control audit.

Appendix E: Coupling dependence of the fitted coefficients

This appendix reports the coefficient-surface SVD, the held-out- κ prediction table, and coefficient-smoothness figures used in Sec. IV D.

1. Coupling SVD protocol and rank summary

For a basis with K operators and N_t time nodes, we stack

$$C_{(n,j),a} = c_n(t_j, \kappa_a).$$

We compare raw coefficient SVD, operator-norm-normalized SVD, and sampler-level rank truncations. Rank-one rescaling is tested both as a reference-point rescaling and as an optimal SVD rank-one surface; in both cases it fails at the sampler level on U_4 , $G(2)$, and $S(k_{\text{min}})$. Adding the next singular directions improves the rollout observables, with the useful rank depending on the observable. The full energy fractions and rank-one rollout failures are given in Table VII.

TABLE VII. Low-rank structure of the coupling-coefficient surface $C_{(n,t),\kappa}$ at $L=8$, $\lambda=0.022$, six κ values. The first two columns give the squared-Frobenius energy fractions retained by the leading and the leading three singular directions; the last column gives rolled-out observables of the optimal rank-one SVD truncation, to be compared with the HMC reference $U_4^{\text{HMC}} \approx 0.494$, $\chi^{\text{HMC}} \approx 59$. The rank-one diagnostic captures most coefficient energy but still produces an order-of-magnitude sampler failure.

Coefficient stack	Rank-1 energy	Rank-3 energy	Rank-1 sampler failure
Operator-norm normalized	92 %	> 99 %	$U_4 \simeq -9 \times 10^{-4}$, $\chi \simeq 1.3$
Raw coefficients	96 %	> 99 %	diagnostic only

2. Held-out- κ prediction table

The full per-observable holdout- κ prediction numbers backing Sec. IV D are given in Table VIII. The HMC and UNet columns there use a separate 2000-sample HMC re-run and are not bit-identical to the canonical 8000-sample reference of Table II; the relative errors quoted in the main text are computed against this independent holdout- κ HMC reference.

TABLE VIII. Holdout- κ prediction at $\kappa^* = 0.27$. Coefficients are fitted on five anchor couplings and interpolated to the held-out point. The last two columns show relative error versus HMC.

Observable	HMC	UNet@ κ^*	Linear interp.	Cubic interp.	Δ_{lin}	Δ_{cubic}
$\langle M \rangle$	0.8986	0.8791	0.8015	0.7846	-10.8%	-12.7%
U_4	0.5065	0.5086	0.4234	0.4162	-16.4%	-17.8%
χ	61.6409	59.0892	54.1264	52.1504	-12.2%	-15.4%
$\langle S \rangle / V$	0.3803	0.3677	0.3628	0.3689	-4.6%	-3.0%

3. Smoothness of the coupling-coefficient surface

The $\phi_{|n|^2=1}^\perp$ coupling sweep is summarized in Fig. 8. The representative coefficient curves used to support the smoothness statement in Sec. IV D are shown in Fig. 9.

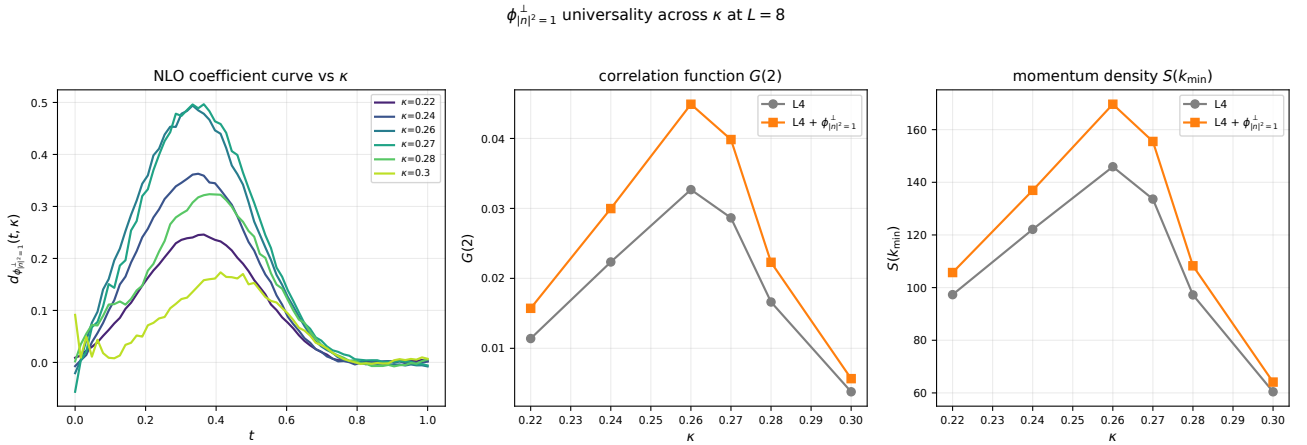


FIG. 8. Six- κ coupling-dependence of $\phi_{|n|^2=1}^\perp$ at $L=8$. The coefficient curve varies smoothly with κ , and the operator improves $G(2)$ and $S(k_{\min})$ across the sweep.

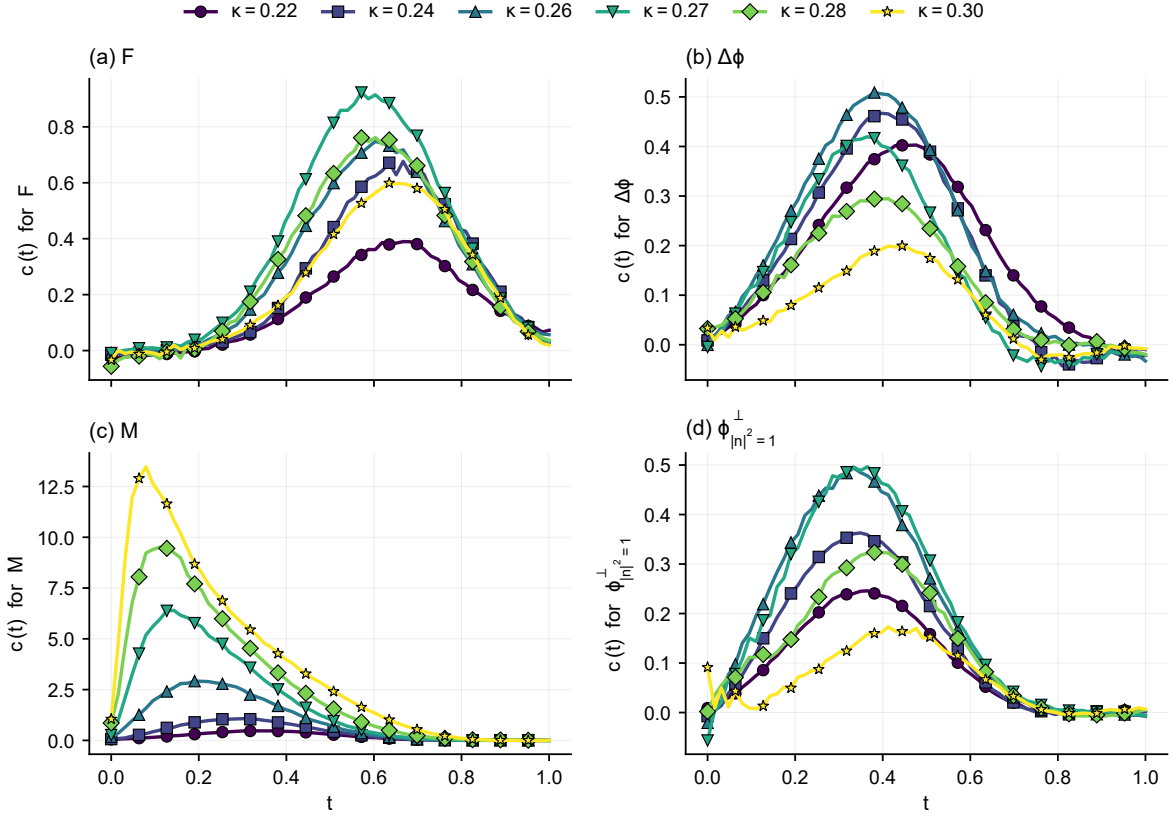


FIG. 9. Smoothness of projection-coefficient curves over the six- κ family. Shown are fitted coefficient functions $c_n(t, \kappa)$ for four representative operator sectors in the $\mathcal{B}_{L4} + \phi_{|n|^2=1}^\perp$ basis: the local force F , the Laplacian stencil $\Delta\phi$, the zero mode M , and the deflated lowest shell $\phi_{|n|^2=1}^\perp$. Each panel uses its own vertical scale. The coefficient curves are smooth in both t and κ , which supports using the same operator basis across the coupling sweep.

Appendix F: Volume transfer and the $L = 16$ ladder

The first test applies $L = 8$ coefficients on $L = 16$ after redefining the operators on the target lattice. This tests coefficient transfer and fails. The second test refits coefficients on $L = 16$ using the same operator classes. This tests operator-class transfer and identifies the same active channels as at $L = 8$ (P_5 and $\phi_{|n|^2=1}^\perp$), while the rematched $L = 16$ sampler still leaves substantial residuals in the same observables. The final test adds $P_7(M; t)$ and $\phi_{|n|^2=2}^\perp$ to test remaining U_4 and finite- k residuals.

1. Cross-size visualization of operator-class transfer

The cross-size visualization supporting the operator-class transfer statement of Sec. IV D is shown in Fig. 10.

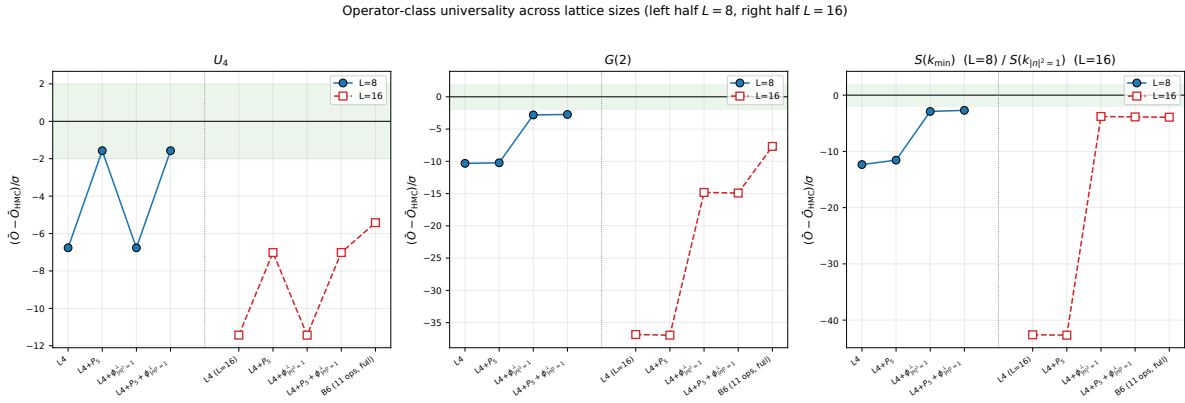


FIG. 10. Cross-size comparison. The same operator classes appear at $L = 8$ and $L = 16$, but the coefficient curves and concrete infrared projectors are volume dependent.

TABLE IX. Sampler observables for the reverse-KL normalizing-flow audit of Sec. VI ($L = 8$, $\kappa = 0.27$, $\lambda = 0.022$, 4096 samples per row). Susceptibility is $\chi_{\text{sign}} = V(\langle M^2 \rangle - \langle M \rangle^2)$.

flow	$P(M > 0)$	$\langle M \rangle$	$\langle M \rangle$	χ_{sign}	U_4
A	0.001	-1.011	1.011	4.99	0.586
B	0.490	-0.018	0.995	68.04	0.588
C	0.490	-0.018	0.999	68.29	0.591
HMC	0.504	+0.025	0.876	59.07	0.494

2. Predefined $L = 16$ NLO ladder

Figure 11 reports the predefined $L = 16$ ladder used after the coefficient-transfer test. Six rungs are shown: the $L4$ baseline, zero-mode extensions through P_5 and P_7 , soft-shell extensions through $|n|^2 = 1$ and $|n|^2 = 2$, and their combined basis. The result is channel-selective: P_7 tightens the Binder channel, while $\phi_{|n|^2=2}^\perp$ moves the next soft shell toward HMC. Residual HMC offsets remain after the final rung.

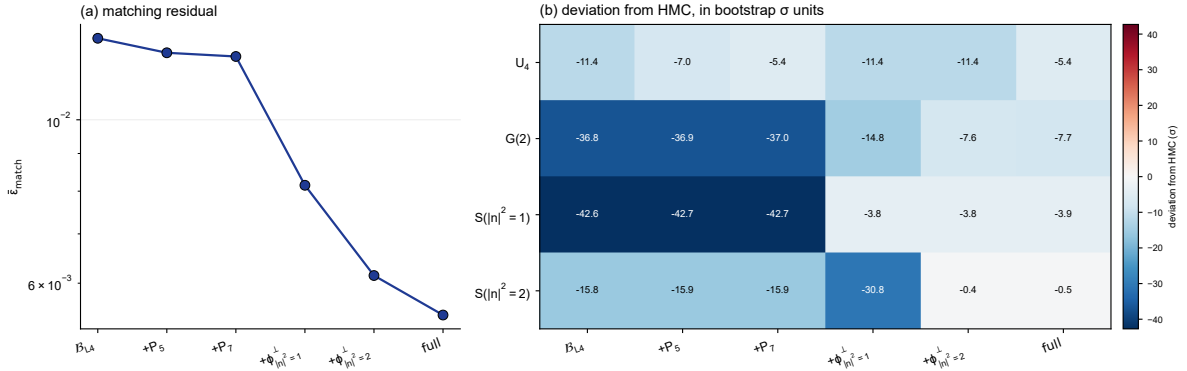


FIG. 11. Predefined $L = 16$ NLO ladder. $P_7(M; t)$ further reduces the Binder-channel deviation, while $\phi_{|n|^2=2}^\perp$ reduces the next soft-shell deviation. Residual HMC offsets remain after the final rung.

Appendix G: Reverse-KL normalizing-flow audit tables

Sampler observables. Table IX lists the sector-balance and Binder-cumulant diagnostics on 4096 samples for the three flows and the HMC reference discussed in Sec. VI.

Appendix H: Training and model details

This appendix records the model and training information needed to interpret the projection audits. Exact optimizer settings, checkpoint names, random seeds, and artifact hashes are part of the release manifest; the table here keeps the manuscript-level audit self-contained.

TABLE X. Training and audit inventory for the learned objects projected in the paper. “Audit distribution” is the distribution on which the operator projection is evaluated, not necessarily the sampler rollout distribution.

System	Learned object	Model / path	Training data	Audit distribution
ϕ^4 FM	$v_\theta(t, \phi)$	straight-flow FlowUNet	HMC at $L = 8$, selected κ, λ	held-out interpolated $\rho_{\text{match}}(t)$
ϕ^4 DM	$s_\theta(\sigma, \phi)$	conditional VE diffusion teacher	HMC at $L = 8$, $\kappa \in \{0.26, 0.27, 0.28\}$	held-out noised data at σ
ϕ^4 NF	ΔS_q	reverse-KL normalizing flows	$L = 8$, $\kappa = 0.27$, $\lambda = 0.022$	HMC evaluation ensemble
U(1) gauge	gauge tangent field	U1EquivNet, VE DSM	$L = 8$, scanned β	held-out noised gauge batch
SU(2) gauge	gauge tangent field	SU2EquivNet, VE DSM	$L = 6$, scanned β	held-out noised gauge batch

Appendix I: Gauge reference ensembles

For $U(1)$ we benchmark the rebuilt HMC against the single-plaquette / infinite-volume Bessel-ratio reference for the Wilson action $S = -\beta \sum_p \cos \theta_p$:

$$\langle \cos \theta_p \rangle_{\text{exact}} = \frac{I_1(\beta)}{I_0(\beta)}, \quad (\text{I1})$$

where I_n is the modified Bessel function of the first kind. For $SU(2)$ we use the action $S = -\frac{\beta}{2} \sum_p \text{Re Tr } U_p$; the single-plaquette / infinite-volume analytic value

$$\langle \frac{1}{2} \text{Tr } U_p \rangle_{\text{exact}} = \frac{I_2(\beta)}{I_1(\beta)} \left[= \frac{I_0(\beta)}{I_1(\beta)} - \frac{2}{\beta} \right] \quad (\text{I2})$$

(the right-hand equality is the Creutz form [21]) is evaluated by direct numerical integration of the Haar-weighted plaquette integral. Both expressions are the single-plaquette / infinite-volume limits of the full character sum on a finite periodic torus; the corresponding finite-volume character-sum correction at the lattice sizes used here ($L=6-8$) is numerically small compared with the sampler-level biases of Sec. VII, but we have not evaluated it analytically. We therefore use the Bessel-ratio expressions only as sanity references against which to validate the HMC implementation, not as the training-set HMC means; the latter are the per-dataset HMC sample means reported in Table XII.

Two independent chains are run at every (L, β) , the integrated autocorrelation time is estimated by the standard cut-at-first-negative estimator, and per-chain plaquette means are reported. Table XI shows the result: at every (L, β) the two-chain mean plaquette agrees with the analytic reference to within 0.1%, per-chain values agree to within 0.2%, and $\tau_{\text{int}}(P) \lesssim 1$. These checks validate the gauge reference datasets used in the projection audits of Sec. VII.

TABLE XI. HMC / heatbath sanity checks for the gauge stress tests of Sec. VII. Column $\langle P \rangle_{\text{HMC}}$ is the mean plaquette over the combined two-chain pool with jackknife error in parentheses (last digit), τ_{int} is the integrated autocorrelation time on chain 1 (cut at first negative bin), and the last two columns report independent-chain plaquette means as a chain-to-chain consistency check. Exact U(1) plaquette uses the lattice Bessel ratio; exact SU(2) plaquette uses $I_0(\beta)/I_1(\beta) - 2/\beta$.

system	L	β	$\langle P \rangle_{\text{HMC}}$	exact	rel.diff	τ_{int}	chain1	chain2
U(1)	8	2.0	0.6975(5)	0.6978	0.03%	0.54	0.6973	0.6978
U(1)	8	4.0	0.8633(2)	0.8635	0.03%	0.53	0.8631	0.8635
SU(2)	6	2.0	0.4334(15)	0.4331	0.06%	0.85	0.4330	0.4338

The dedicated two-chain SU(2) sanity pool gives $\langle P \rangle = 0.4334(15)$ at $L=6$, $\beta=2$, while the single 4096-sample HMC chain used as the training and matching dataset for the SU(2) audit of Table XII reads 0.4297. The gap is about 0.9% and is consistent with the expected chain-to-chain dispersion of a 4096-step pool at this τ_{int} ; we report the audit-chain value in Table XII so that teacher and representation biases are read against the dataset they were trained or matched on, and the two-chain sanity value here so that the analytic Bessel ratio is verified independently.

Appendix J: Gauge projection and rollout observables

This appendix reports the rolled-out gauge observables and the architecture–projection overlap audit used in Sec. VII.

1. Wilson-loop observables and topology

We sample from each trained teacher by a variance-exploding rollout (Heun integrator with Karras-style stochastic churn for U(1); pure Heun for SU(2)) and from each representation sampler by replacing the network output with the matched coefficient combination. Mean plaquette and 1×2 , 2×2 Wilson loops are shown in Fig. 12; the per-system summary of held-out matching residuals together with rolled-out plaquettes is collected in Table XII.

TABLE XII. Gauge projection summary. Wilson-loop-force operators reduce the per-step matching residual relative to the plaquette baseline, while negative controls do not. The rolled-out plaquette columns report sampler-level offsets for the trained teachers and representation samplers. $\bar{\epsilon}[\mathcal{B}_0]$ and $\bar{\epsilon}_{\text{best}}^{\text{loop}}$ report the per-step matching residual on the deepest loop-force rung of the nested ladder (\mathcal{B}_3 for U(1) and \mathcal{B}_2 for SU(2)), while the last rollout column reports the canonical three-operator \mathcal{B}_2 representation for cross-system comparability. SU(2) teacher and representation values are mean \pm standard deviation over three audit-RNG seeds on the same trained teacher.

System	$\bar{\epsilon}_{\text{gauge}}$	$\bar{\epsilon}[\mathcal{B}_0]$	$\bar{\epsilon}_{\text{best}}^{\text{loop}}$	$\bar{\epsilon}_{\text{best}}^{\text{neg}}$	$\langle P \rangle_{\text{HMC}}$	Teacher rollout	canonical \mathcal{B}_2 rollout
U(1), $\beta = 2$	9.1×10^{-5}	0.502	0.420	0.502	0.6972	0.6497	0.5894
U(1), $\beta = 4$	6.9×10^{-5}	0.578	0.246	0.578	0.8644	0.7613	0.6700
SU(2), $\beta = 2$	3.7×10^{-4}	0.271	0.251	0.271	0.4297	0.4006 ± 0.0024	0.3810 ± 0.0025

Table XII also reports rolled-out plaquettes. The trained gauge teachers are 7–12% below HMC, and the canonical \mathcal{B}_2 representations are 11–23% below HMC. Longer Wilson loops in Fig. 12 show the same trend: \mathcal{B}_2 tracks the teacher more closely than \mathcal{B}_0 . The U(1) topological charge remains integer-valued, while χ_Q is over-dispersed by a factor of 2–3.

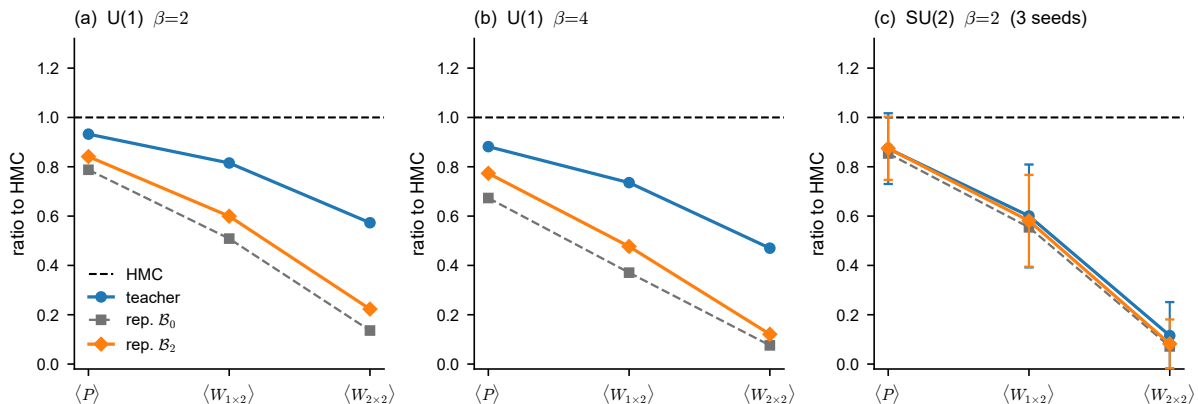


FIG. 12. Wilson-loop observables as ratios to HMC. The trained gauge teachers are biased relative to HMC, and the \mathcal{B}_2 representation tracks the teacher more closely than the plaquette-only \mathcal{B}_0 but remains biased. The panels show the sampler-level Wilson-loop offsets associated with the tangent-field truncation. SU(2) error bars are the standard deviation over three audit-RNG seeds on the same trained teacher.

2. Architecture–projection overlap audit

The architecture–projection overlap audit summarized in Sec. VII E is reproduced as Table XIII.

TABLE XIII. Architecture–projection overlap audit. Hard-coded primitives denote the symmetry-restricted output basis recorded for the checkpoint where available; the table should be read as an architecture audit, not as proof that a listed sector was discovered outside the network basis.

System	Symmetry	Output primitives / wrapper	Projection loading / controls
ϕ^4 FlowUNet	none / soft Z_2	local stencils only	$M, M^3, P_5, \phi_{ n ^2=1}^\perp$
ϕ^4 hard- Z_2	global Z_2	odd-projection wrapper	$M, M^3, P_5, \phi_{ n ^2=1}^\perp$
U(1) U1EquivNet	local U(1)	$V_P, V_R, V_{P^2}, V_{Pol}$	$V_{2 \times 2}, V_{ n ^2=1}^\perp$ diagnostics
SU(2) SU2EquivNet	local SU(2)	checkpoint-dependent loop-force primitives	V_{adjP} dominant; V_R tested but weak; controls fail

Appendix K: Gauge coupling sweep

We repeat the gauge projection audit at additional couplings while holding the architecture, optimizer, dataset size, and projection basis fixed. These sweeps test whether the loop-force hierarchy and the failure of the controls persist away from the main couplings; they are not separately optimized sampler benchmarks.

1. U(1) coupling sweep

For compact U(1) gauge theory with Wilson action [22] $S[U] = -\beta \sum_p \cos \theta_p$, we train the same gauge-equivariant DSM teacher at $\beta \in \{1.0, 2.0, 4.0, 6.0\}$, $L = 8$, using 4096 HMC samples and the same variance-exploding noise range as in the main text. The Wilson-loop-force ladder is $\mathcal{B}_0 = \{V_P\}$, $\mathcal{B}_1 = \{V_P, V_R\}$, $\mathcal{B}_2 = \{V_P, V_R, V_{P^2}\}$, $\mathcal{B}_3 = \{V_P, V_R, V_{P^2}, V_{Pol}\}$. At every coupling the gauge-equivariance violation remains at the numerical-audit floor, $\bar{\epsilon}_{\text{gauge}} \sim 7 \times 10^{-5} - 2 \times 10^{-4}$ across $\beta \in \{1, 2, 4, 6\}$. The three standard controls—the gauge-variant raw link θ_l , a random tangent field, and a shuffled-stencil plaquette force—reduce the plaquette-only residual by less than 0.1% at every β . In contrast, the full Wilson-loop-force ladder \mathcal{B}_3 reduces the held-out matching residual relative to \mathcal{B}_0 by 2.6%, 16.4%, 57.4%, and 4.6% at $\beta = 1, 2, 4, 6$, respectively. The improvement is largest at intermediate coupling: at strong coupling the score is dominated by noise structure, while at weak coupling the linearized plaquette force already captures most of the tangent field.

The teacher reproduces the mean plaquette to 3.5%, 6.8%, 11.8%, and 4.0% at the same four couplings, relative to the HMC reference. Larger Wilson loops follow the HMC area-law slope across the sweep, but the teacher systematically undershoots the exponentially small large-loop tail.

2. SU(2) coupling sweep

For SU(2) gauge theory with Wilson action $S[U] = -\frac{\beta}{2} \sum_p \text{Re Tr } U_p$, we train the same SU(2)-equivariant DSM teacher at $\beta \in \{1.5, 2.0, 3.0\}$, $L = 6$, with Wilson-loop-force ladder $\mathcal{B}_0 = \{V_P\}$, $\mathcal{B}_1 = \{V_P, V_R\}$, $\mathcal{B}_2 = \{V_P, V_R, V_{\text{adjP}}\}$. At every coupling the gauge-equivariance violation remains below $\bar{\epsilon}_{\text{gauge}} \lesssim 4 \times 10^{-4}$ across $\beta \in \{1.5, 2, 3\}$. The adjoint-plaquette-augmented basis \mathcal{B}_2 reduces the held-out matching residual relative to \mathcal{B}_0 by 5.5%, 7.4%, and 5.6% at $\beta = 1.5, 2.0, 3.0$, respectively. The rectangle operator V_R alone contributes $\lesssim 0.7\%$, identifying V_{adjP} as the dominant non-plaquette loading in the scanned range. The three negative controls—raw-link projection, random Lie-algebra field, and shuffled-staple operator—reduce the residual by less than 0.05% at every coupling.

The trained teacher tracks the HMC mean plaquette to 12.5%, 6.9%, and 5.9% at the same three couplings. As in the U(1) case, large Wilson loops reproduce the qualitative area-law trend but remain biased in absolute magnitude. The coupling sweep is summarized in Fig. 13 and Table XIV.

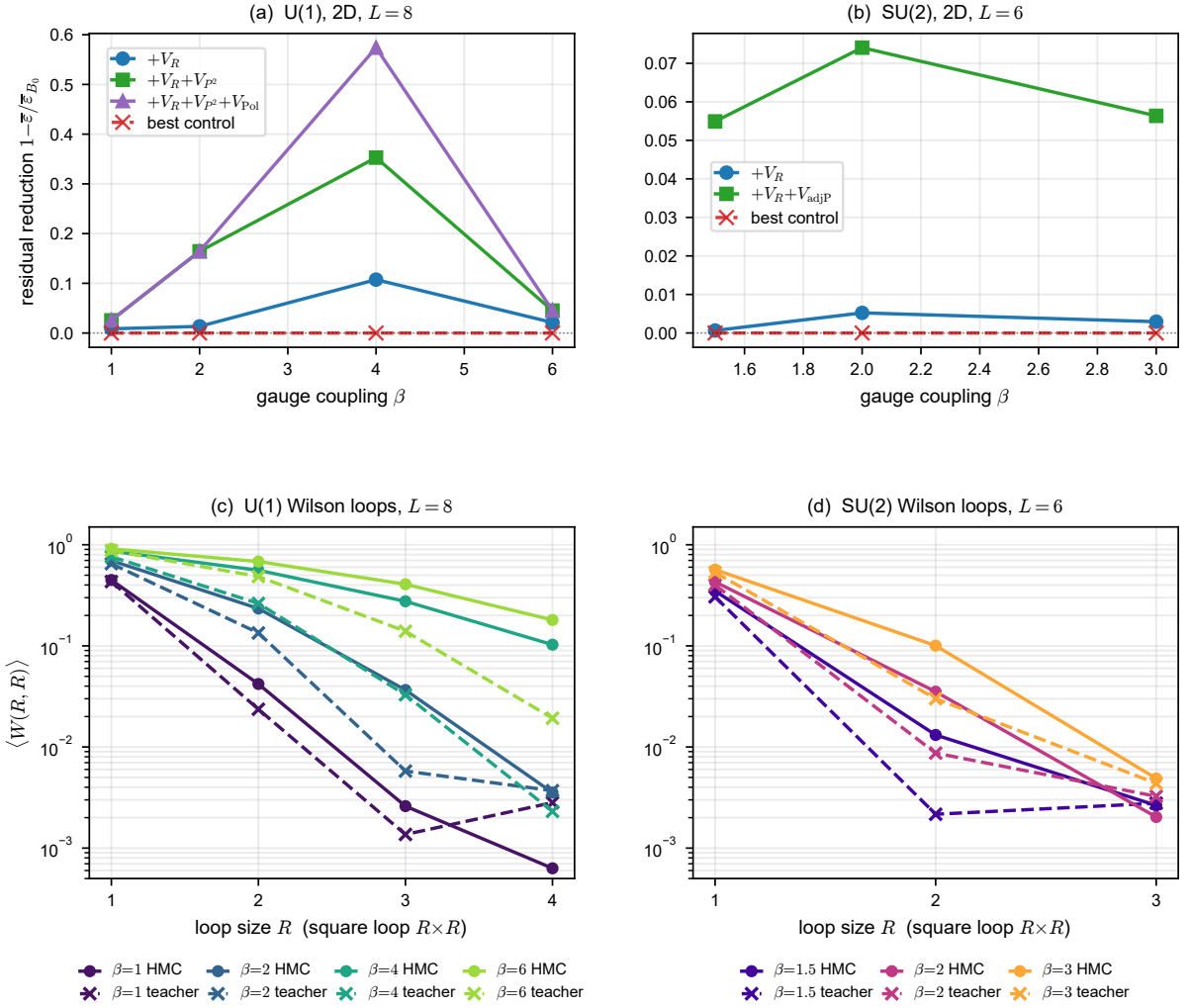


FIG. 13. Gauge coupling sweep. (a) U(1), $L = 8$: residual reduction $1 - \bar{\epsilon}/\bar{\epsilon}_{\mathcal{B}_0}$ for the Wilson-loop-force ladder and the best negative control as a function of β . (b) SU(2), $L = 6$: residual reduction for $\mathcal{B}_1 = \{V_P, V_R\}$, $\mathcal{B}_2 = \{V_P, V_R, V_{adjP}\}$, and the best negative control. Across both gauge groups the Wilson-loop-force ladder remains separated from the control band at every coupling tested. (c,d) Square Wilson loops $\langle W(R, R) \rangle$ versus loop size R for HMC and the trained DSM teacher, shown on a log scale. The teacher reproduces the qualitative area-law slope but undershoots the large-loop tail.

TABLE XIV. Gauge coupling sweep summary. The residual reduction is measured relative to the plaquette-force baseline \mathcal{B}_0 . The “best control” column reports the largest reduction among the negative controls at that coupling.

System	β	$\bar{\epsilon}_{\text{gauge}}$	Wilson-loop-force ladder reduction	Best control reduction	Teacher plaquette error
U(1), $L = 8$	1.0	9.8×10^{-5}	2.6%	< 0.1%	3.5%
U(1), $L = 8$	2.0	9.1×10^{-5}	16.4%	< 0.1%	6.8%
U(1), $L = 8$	4.0	7.0×10^{-5}	57.4%	< 0.1%	11.8%
U(1), $L = 8$	6.0	1.6×10^{-4}	4.6%	< 0.1%	4.0%
SU(2), $L = 6$	1.5	2.7×10^{-4}	5.5%	< 0.1%	12.5%
SU(2), $L = 6$	2.0	3.7×10^{-4}	7.4%	< 0.1%	6.9%
SU(2), $L = 6$	3.0	2.8×10^{-4}	5.6%	< 0.1%	5.9%

Appendix L: U(1) non-primitive operator extension

The U(1) loop-force ladder in Sec. VII partially overlaps with the gauge-covariant primitives exposed by the architecture. To test whether the projection can expose directions beyond these built-in primitives, we add two

non-primitive operators that are not hard-coded as output basis elements of the network.

The first is the 2×2 Wilson-loop force

$$V_{2 \times 2}(l) = -\frac{\partial}{\partial \theta_l} \sum_{C_{2 \times 2}} \cos \theta_C, \quad (\text{L1})$$

where the sum is over all 2×2 loops. The second is a soft magnetic-shell force

$$V_{|n|^2=1}^{\text{sh}} = -d^\dagger \Pi_{|n|^2=1} \sin \theta_p, \quad (\text{L2})$$

the gauge analogue of the scalar soft-shell field $\phi_{|n|^2=1}^\perp$.

Extending the canonical U(1) ladder from \mathcal{B}_3 to $\mathcal{B}_5 = \mathcal{B}_3 \cup \{V_{2 \times 2}, V_{|n|^2=1}^{\text{sh}}\}$ changes the held-out per-step matching residual by less than 1.2% at every coupling tested. Thus the local score residual is already largely captured by the canonical four-operator ladder. The rollout tells a different story: adding $V_{2 \times 2}$ produces a much larger change in non-local Wilson loops, moving the representation sampler toward both the teacher and HMC targets in Table XV. The correction remains partial, and $V_{|n|^2=1}^{\text{sh}}$ gives only marginal further improvement. This separates local per-step score matching from the sensitivity of extended Wilson loops to non-primitive operators.

TABLE XV. U(1) non-primitive operator extension. Adding the 2×2 Wilson-loop force $\mathcal{B}_4 = \mathcal{B}_3 + V_{2 \times 2}$ moves rolled-out non-local Wilson loops toward both the teacher and HMC targets, but leaves a remaining gap. ‘‘Gain’’ is $\mathcal{B}_4 - \mathcal{B}_3$, and ‘‘Rel. gain’’ is this increase relative to \mathcal{B}_3 .

System	Observable	HMC	Teacher	\mathcal{B}_3	\mathcal{B}_4	Gain	Rel. gain
U(1), $\beta = 4$	$W_{2 \times 2}$	0.560	0.263	0.063	0.125	0.062	98%
U(1), $\beta = 4$	$W_{2 \times 3}$	0.421	0.119	0.011	0.039	0.028	255%
U(1), $\beta = 6$	$W_{2 \times 2}$	0.683	0.486	0.162	0.243	0.081	50%
U(1), $\beta = 6$	$W_{2 \times 3}$	0.560	0.305	0.043	0.106	0.063	147%

Appendix M: Finite-step blocking caveat

The smooth coefficient surface $c_n(t, \kappa, L)$ in the main text is a set of projection coordinates of the trained generative object. The blocking pilot only identifies candidate operator classes for a later finite-step matching study; a quantitative blocking analysis would require a closed blocking map, a conditional (κ, L) teacher, and an operator-mixing matrix on the induced blocked measures.

-
- [1] S. Duane, A. D. Kennedy, B. J. Pendleton, and D. Roweth, *Phys. Lett. B* **195**, 216 (1987).
 - [2] N. Metropolis, A. W. Rosenbluth, M. N. Rosenbluth, A. H. Teller, and E. Teller, *J. Chem. Phys.* **21**, 1087 (1953).
 - [3] M. S. Alberg, G. Kanwar, and P. E. Shanahan, *Phys. Rev. D* **100**, 034515 (2019).
 - [4] G. Kanwar, M. S. Alberg, D. Boyda, K. Cranmer, D. C. Hackett, S. Racanière, D. J. Rezende, and P. E. Shanahan, *Phys. Rev. Lett.* **125**, 121601 (2020).
 - [5] K. A. Nicoli, C. J. Anders, L. Funcke, T. Hartung, K. Jansen, P. Kessel, S. Nakajima, and P. Stornati, *Phys. Rev. Lett.* **126**, 032001 (2021).
 - [6] Y. Lipman, R. T. Q. Chen, H. Ben-Hamu, M. Nickel, and M. Le, in *International Conference on Learning Representations* (2023).
 - [7] X. Liu, C. Gong, and Q. Liu, in *International Conference on Learning Representations* (2023) [arXiv:2209.03003](https://arxiv.org/abs/2209.03003).
 - [8] D. Boyda, G. Kanwar, S. Racanière, D. J. Rezende, M. S. Alberg, K. Cranmer, D. C. Hackett, and P. E. Shanahan, *Phys. Rev. D* **103**, 074504 (2021).
 - [9] L. Wang, G. Aarts, and K. Zhou, *J. High Energy Phys.* **05**, 060, [arXiv:2309.17082](https://arxiv.org/abs/2309.17082).
 - [10] A. Hyvärinen, *J. Mach. Learn. Res.* **6**, 695 (2005).
 - [11] Y. Song, J. Sohl-Dickstein, D. P. Kingma, A. Kumar, S. Ermon, and B. Poole, in *International Conference on Learning Representations* (2021).
 - [12] J. Ho, A. Jain, and P. Abbeel, in *Advances in Neural Information Processing Systems*, Vol. 33 (2020) pp. 6840–6851.
 - [13] P. Vincent, *Neural Comput.* **23**, 1661 (2011).
 - [14] T. Karras, M. Aittala, T. Aila, and S. Laine, in *Advances in Neural Information Processing Systems*, Vol. 35 (2022) pp. 26565–26577.
 - [15] D. J. Rezende and S. Mohamed, in *Proceedings of the 32nd International Conference on Machine Learning*, PMLR,

- Vol. 37 (2015) pp. 1530–1538.
- [16] L. Dinh, J. Sohl-Dickstein, and S. Bengio, in *International Conference on Learning Representations* (2017) [arXiv:1605.08803](#).
- [17] G. Papamakarios, E. Nalisnick, D. J. Rezende, S. Mohamed, and B. Lakshminarayanan, *J. Mach. Learn. Res.* **22**, 1 (2021).
- [18] T. Minka, *Divergence measures and message passing*, Tech. Rep. MSR-TR-2005-173 (Microsoft Research, 2005).
- [19] T. S. Cohen and M. Welling, in *Proceedings of the 33rd International Conference on Machine Learning*, PMLR, Vol. 48 (2016) pp. 2990–2999, [arXiv:1602.07576](#).
- [20] K. Binder, *Z. Phys. B* **43**, 119 (1981).
- [21] M. Creutz, *Phys. Rev. D* **21**, 2308 (1980).
- [22] K. G. Wilson, *Phys. Rev. D* **10**, 2445 (1974).